MOX-Report No. 48/2017

Active contraction of cardiac cells: a reduced model for sarcomere dynamics with cooperative interactions

Regazzoni, F.; Dedè, L.; Quarteroni, A.

MOX, Dipartimento di Matematica
Politecnico di Milano, Via Bonardi 9 - 20133 Milano (Italy)

mox-dmat@polimi.it http://mox.polimi.it

Active contraction of cardiac cells: a reduced model for sarcomere dynamics with cooperative interactions

Francesco Regazzoni*[1], Luca Dedè[1], Alfio Quarteroni[1,2]

[1] *MOX - Dipartimento di Matematica, Politecnico di Milano, P.zza Leonardo da Vinci 32, 20133 Milano, Italy*
[2] *CMCS-MATH-SB, Ecole Polytechnique Fédérale de Lausanne, Av. Piccard, CH-1015 Lausanne, Switzerland*

Abstract

We propose a reduced ODE model for the mechanical activation of cardiac myofilaments, which is based on explicit spatial representation of nearest-neighbour interactions. Our model is derived from the cooperative Markov Chain model of Washio et al. 2012, under the assumption of conditional independence of specific sets of events. This physically motivated assumption allows to drastically reduce the number of degrees of freedom, thus resulting in a significantly large computational saving. Indeed, the original Markov Chain model involves a huge number of degrees of freedom (order of 10^{21}) and is solved by means of the Monte Carlo method, which notoriously reaches statistical convergence in a slow fashion. With our reduced model, instead, numerical simulations can be carried out by solving a system of ODEs, reducing the computational time by more than 10 000 times. Moreover, the reduced model is accurate with respect to the original Markov Chain model. We show that the reduced model is capable of reproducing physiological steady-state force-calcium and force-length relationships with the observed asymmetry in apparent cooperativity near the calcium level producing half activation. Finally, we also report good qualitative and quantitative agreement with experimental measurements under dynamic conditions.

1 Introduction

A distinctive feature of living matter is that the stress is not uniquely determined by the strain since muscle tissues are intrinsically able to generate force (Bers 2001). Modelling the process behind the active contraction of cardiomyocytes is crucial for understanding heart functionality, since it represents the natural bridge between electrophysiology and mechanics.

Cardiomyocytes, the cardiac muscle cells, are composed by myofibrils, long bundles of sarcomeres, the cell contractile units, surrounded by sarcoplasmic reticulum and delimited by Z disks (see Figure 1). Each sarcomere contains thick filaments (myosin filaments, MFs) and thin filaments (actin filaments, AFs), which are anchored to Z disks. Myosin molecules are composed of a head, which is capable of binding to actin, a neck and a tail. Myosin heads (MHs) are distributed along the thick filament, but for

*Corresponding author. Email address: `francesco.regazzoni@polimi.it`

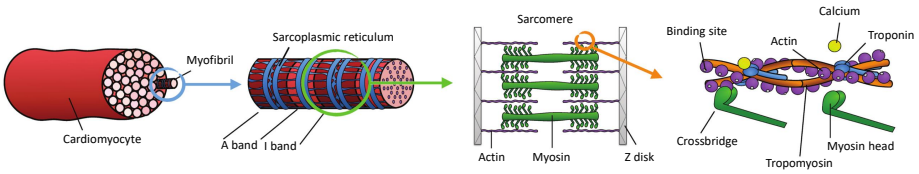

Figure 1: Inner structure of cardiomyocytes.

a narrow region, named H-zone and located at the centre of the filament. During cell depolarization, the increment of calcium ions concentration inside the cells induces the release of the calcium stored in the sarcoplasmic reticulum, thus triggering the binding between troponin C and Ca^{2+}. This chemical reaction causes a configuration change of the protein tropomyosin, thus exposing the binding sites for myosin heads; the latter bind to actin, forming the so called crossbridges (XBs), thus leading to the sliding between the two filaments. At the macroscale, the consequence of such so-called crossbridge mechanism is the muscle contraction (Bers 2001; Keener and Sneyd 2009; Quarteroni et al. 2017).

1.1 Unregulated models

The earliest attempts to model the tension development in muscle tissues are based on the experimental work of Hill on quick release from isometric condition of tetanized skeletal frog muscle (Hill 1938). This model incorporates a phenomenological description of the force-velocity relationship. However, it is not suited for the cardiac muscle, since tetanized contractions are not common in the heart. Moreover, Hill's model does not incorporate the coupling with electrophysiological quantities such as calcium concentration. The model can therefore be regarded as an empirical law neglecting biophysical phenomena (Fung 2013; Sachse 2004).

Most of current models of tension development are based on the sliding filaments theory, proposed independently in 1954 by two research teams (Huxely and Niedergerke 1954; Huxely and Hanson 1954). The original model (Huxely 1957) contains only two states for XBs, attached and detached, with transition rates dependent on the relative position of the actin-binding site to the equilibrium position of the nearest MH. The force is represented as a linear function of distortion of attached XBs, which act as linear springs. The first numerical simulations based on this theory were performed with the model proposed in Wong 1971, which has been improved in later works to match thermodynamical self-consistency (Eisenberg and Hill 1985; Hill et al. 1975; Pate and Cooke 1986).

1.2 Regulated mean-field models

The models previously mentioned do not incorporate the calcium-based regulation of activation, and are thus limited to the condition of full activation. More recent models incorporate the description of troponin-tropomyosin regulatory units (RU) to account for the effect of calcium ions concentration on cross bridge formation (Landesberg and Sideman 1994; Razumova, Bukatina, and Campbell 1999; Rice, Winslow, and Hunter 1999; Sachse, Glänzel, and Seemann 2003).

By adopting a mean-field approach, a single representative RU or XB (or a couple RU/XB) is described by a Continuous-Time Markov Chain (CTMC) or Markov Jump

process (see Norris 1998), with a finite number of states. The states included in the CTMC depend on the level of complexity of the model and on which components are either comprised or neglected in the description (the most popular choices are the calcium-binding state of troponin C, the permissivity of tropomyosin, and the binding state of XBs) and their number range from 3 (see for instance Hussan, Tombe, and Rice 2006) to more than 10 (see Sachse, Glänzel, and Seemann 2003). The calcium-based regulatory system is incorporated by making the transition rates of the states describing the RUs dependent on intracellular calcium ions concentration.

Thanks to the small number of states of the Markov Chain, the solution of such models can be obtained by solving the associated Forward Kolmogorov Equation (FKE). The FKE, also known as Master Equation in natural sciences, describes the time evolution of the probabilities associated with the states in the phase space of a random process (Bailey 1990). When the underlying random process is a CTMC, the associated FKE is a system of ODEs, with as many variables as the number of states of the CTMC. This provides an expression for the probability of the tension generating states, which in turns gives the generated force. To account for the effect of sarcomere length (SL), the expression of the force is typically multiplied by the so-called *sarcomere overlap function*, which quantifies the fraction of MHs recruitable for tension generation, as the fraction of MHs facing a single AF (Landesberg and Sideman 1994; Rice, Winslow, and Hunter 1999; Sachse 2004; Trayanova and Rice 2011).

1.3 Cooperative interactions

A prominent feature of the cardiac tissue is the anomalously high (with respect to the skeletal muscle) sensitivity of the developed force to calcium concentration. The steeply nonlinear response to activator calcium ions can be explained by the cooperative interactions inside sarcomeres, even if a debate about the exact cooperativity mechanism is still ongoing (see e.g. Dupuis et al. 2016). Three theories have been proposed, not mutually exclusive: the first one (named XB-RU) assumes that the attachment of a XB increases the affinity of troponin C to calcium ions; the second one (XB-XB) is that attached XBs increase the rate of formation of nearby XBs; the third one (RU-RU) is that the transition of a tropomyosin molecule to the permissive state facilitates the same transition for neighbouring molecules by means of end-to-end interactions (Brandt et al. 1987).

To account for cooperative mechanisms in mean-fields models, different strategies have been employed (Rice, Winslow, and Hunter 1999; Sachse 2004). While the XB-RU cooperativity hypothesis can be easily modelled by increasing the calcium-binding rate when the RU is involved in a XB, the XB-XB and RU-RU interactions are difficult to be rigorously incorporated in a mean-field framework. Nevertheless, numerical comparisons of the effect of the three putative cooperative mechanisms highlighted that RU-RU interactions are crucial to reproduce most of the experimentally observed behaviours, such as steady-state force-calcium relationship and twitch contractions (Rice, Winslow, and Hunter 1999).

As an attempt to incorporate end-to-end interactions into mean-field models, the transition rate of RUs from the non-permissive state to the permissive one was assumed to be an increasing function of the concentration of permissive RUs (i.e. of the probability associated with the permissive states); on the other hand, the reverse transition rate was assumed to be a decreasing function of the same quantity (Landesberg and Sideman 1994; Rice, Winslow, and Hunter 1999; Sachse 2004). However,

the numerical results for the latter model did not show good agreement with experimental measurements (Rice and Tombe 2004). The missing ingredient to model end-to-end interactions, as highlighted in the seminal work by Rice and De Tombe, is the spatially-explicit description of RUs and/or XBs along the filaments, which cannot be captured by mean-field models. Indeed, in the mean-field framework, the state of *all* units affects the transition rates of *all* units, since a spatially-detailed description is missing (Chabiniok et al. 2016).

To avoid an explicit representation of end-to-end interactions, Rice et al. 2008 proposed a mean-field model whose transition rates were phenomenologically modified to reproduce the steeply nonlinear response of the tissue to calcium concentration. This approach is similar to the one employed in Hunter, McCulloch, and Ter Keurs 1998 and in Niederer, Hunter, and Smith 2006, where the rate of activation is set as a nonlinear function of calcium concentration, such that the steady state solution coincides with the Hill's function (see Eq. (18)). A similar phenomenological model, based on measurements on human cardiomyocytes, is proposed in Land et al. 2017.

1.4 Regulated spatially-explicit models

In Rice et al. 2003 the authors proposed a spatially-explicit model, consisting in a filament of $N = 26$ RUs, each one described by a 4-states CTMC. To account for end-to-end interactions, the transition rates between the permissive and the non-permissive states was assumed to depend on the state of nearest-neighbouring RUs. The numerical simulations of the model showed a great improvement, with respect to mean-field models, in the agreement with experimental observed behaviours, both under steady and dynamic conditions. Moreover, the spatial description of the filament allowed to incorporate the SL-dependence in a more rigorous way than in mean-field models, since the overlap of MFs and AFs can be explicitly incorporated (see Washio et al. 2012).

The drawback of spatially-explicit models is their overwhelming computational complexity: a model comprising N units, each one modelled by a Markov Chain with s states, has s^N total degrees of freedom. This hinders the possibility of numerically solving the FKE associated with such models and thus dictates the use of the time-consuming Monte Carlo (MC) method (Hussan, Tombe, and Rice 2006; Rice and Tombe 2004; Washio et al. 2013, 2015).

Different attempts were pursued to overcome this inconvenient. In Rice et al. 2003 periodic boundary conditions are considered, so that the model reduces to the Ising problem, whose analytical solution is known (Cipra 1987). However, this approach is restricted only to the steady state, and the ring simplification neglects the so-called border-effect in the filament (see Washio et al. 2012). In Campbell et al. 2010 the authors assume periodic boundary conditions for the filament, so that a large number of states can be identified, being defined but for a translation of the filament. This reduces by an order of magnitude the number of states; however, besides the drawback of the ring simplification, this approach can still be applied to a limited number of units, due to its high computational cost.

In Washio et al. 2012 the authors developed a novel method to derive an approximate ODE model starting from the model of Rice et al. 2003, comprising N Markov Chains with 4 states each. They considered the FKE associated with each one of the N units, amounting to a total of $4N$ ODEs. Since the units are mutually coupled, at right-hand side they came across the joint probabilities of triplets of consecutive units, which have to be modelled for model closure. The joint probabilities of triplets

AF	Actin filament	ODE	Ordinary differential equation
MF	Myosin filament	CTMC	Continuous-time Markov Chain
MH	Myosin head	MC	Monte Carlo
XB	Crossbridge	FKE	Forward Kolmogorov Equation
RU	Regulatory unit		

Table 1: Glossary of abbreviations.

was approximated with a function of the probabilities of single units assumed in the past times, ending up with an integro-differential system with memory. This model requires the determination of a number of coefficients, which were estimated with a least square fitting on the results of a collection of MC simulations, obtained with different calcium transients. In spite of the remarkable reduction of complexity, this approach features some drawbacks. It requires a long off-line phase for the estimation of coefficients, to be repeated any time the parameters of the underlying Markov Chain model are modified. Moreover, since the coefficients are fitted for some specific calcium transients, they are not guaranteed to be meaningful under different conditions.

In Land and Niederer 2015, a spatially detailed model incorporating both thin filaments kinetics and XB dynamics is proposed. The model includes $n = 26$ RUs, with allowed "unblocked" and "blocked" states, and $m = 69$ XBs, with allowed "unbound" and "bound" states. To reduce the complexity of the model, the authors identified the state of the model by the number of unblocked RUs and of bound XBs, lowering the number of states down to $(n + 1)(m + 1)$ in place of the original 2^{n+m}. To compute the free energy associated with a given state they had to sum over all possible configurations belonging to that state, for which they combined two reduction techniques. First, they grouped the 2^n thin filament states into 3 010 classes, according to the number and length of adjacent stretches of unblocked RUs, and they considered a single representative state for each class. Then, they computed the sum over all XBs configurations by using a MC approximation by random sampling.

1.5 Our contribution and paper outline

In this work we consider the spatially-explicit CTMC model of sarcomere dynamics presented in Rice et al. 2003, with the modification proposed in Washio et al. 2012. Starting from this model, we consider the FKE associated with the full Markov Chain with $N = 36$ units. This system of ODEs is computationally useless, due to the gigantic number of its degrees of freedom: indeed the unknowns are approximately $5 \cdot 10^{21}$, which would require tens of billions of terabytes of memory just to store the current state. To overcome this difficulty, we consider a smaller set of events (of cardinality smaller then 2 200) and, under a conditional independence hypothesis, we derive an ODE model for the time evolution of the associated probabilities. Then, we compare the results of our reduced model with those of the original model of Washio et al. 2012 and we validate them, also by comparing our results with experimental data in conditions not explored in Washio et al. 2012. This comparison shows that our model, albeit simplified, is still able to reproduce many experimentally observed features, both in the steady and dynamic regimes.

The paper is organized as follows. In Section 2 we recall the Markov Chain model presented in Washio et al. 2012 and the derivation of the associated FKE. In Section 3 we derive and analyse the reduced ODE model. Then we investigate the accuracy

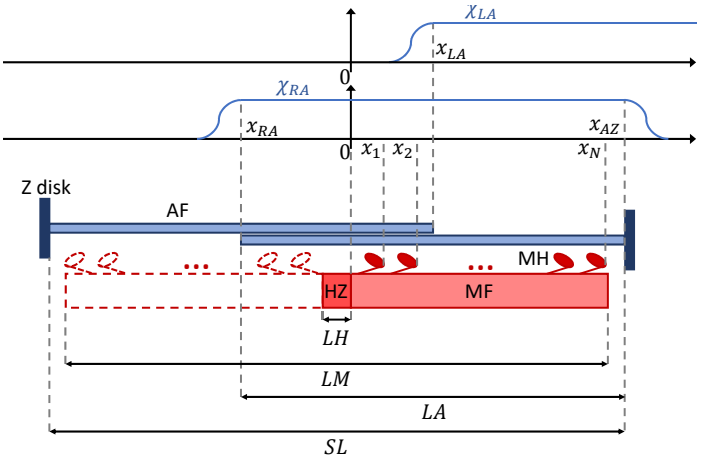

Figure 2: Scheme of the model described in Section 2.1. The thick filament (MF) is represented in red and two thin filaments (AF) are represented in blue (mid). A reference system is placed with the origin at the right-hand side of the H-zone (HZ). The functions χ_{LA} and χ_{RA}, indicating respectively the region at the right of the left AF, and the region covered by the right AF, are represented (top). The length of the H-zone (LH), of the thick filament (LM), of a thin filament (LA), and of the sarcomere (SL) are also depicted (bottom).

of the model and we compare the numerical results with those obtained by means of the MC method. We discuss the possibility of coupling the proposed model with existing models for cardiac electrophysiology on one side and for cardiac mechanics on the other. Section 4 provides the results of some numerical simulations of the model, under both steady and dynamic conditions. Section 5 provides final remarks and outlines for future research.

For reader's convenience, we report in Table 1 a glossary of the abbreviations used in this paper.

2 Sarcomere dynamics: the full model

In this section we illustrate the model of sarcomere dynamics firstly proposed in Rice et al. 2003 and later modified in Washio et al. 2012 to account for the dependence of the dynamics on the elongation of the sarcomere.

2.1 Model description

The sarcomere representation is depicted in Figure 2. The model considers a single thick filament (MF) and two thin filaments (AFs). Thanks to the symmetry of the model, we consider just half sarcomere. The current sarcomere length (SL), which is an input parameter of our model, determines the mutual superimposition between the AFs and the MF. Along the MF, at each side of the H-zone, N myosin heads (MHs) are placed at regular intervals. Depending on SL, each MH can face either no AFs, or a single AF (which is the most favourable condition for XBs to formate), or two AFs.

The state of each MH is determined by the calcium binding state (0 stands for *not bound*, while 1 for *bound*) and XB permissivity ($\mathcal{N}$ stands for *non-permissive*, $\mathcal{P}$

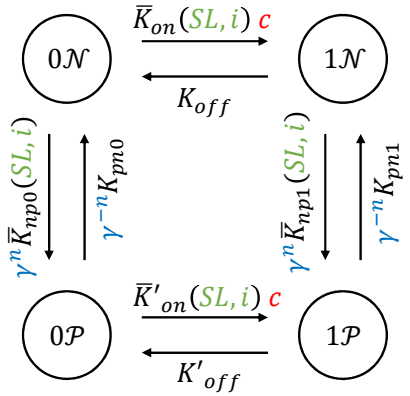

Figure 3: The cooperative four states Markov model. The terms depending on the intra-cellular calcium concentration c are highlighted in red; terms depending on the state of neighbouring MHs (i.e. depending on n) are highlighted in blue; terms depending on the position of the MH and the current sarcomere elongation are highlighted in green.

for *permissive*). The transition rates between the 4 possible states, whose set will be denoted by $\mathcal{S} = \{0\mathcal{N}, 1\mathcal{N}, 0\mathcal{P}, 1\mathcal{P}\}$, are summarized in Figure 3 and depend on the free calcium concentration (high concentrations favour the transition $0 \to 1$), the number of opposite AFs (through the MH index i and the variable SL), and $n \in \{0, 1, 2\}$, namely the number of adjacent heads in permissive state. The last dependence is responsible for the cooperative mechanism: a large value of n favours the transition $\mathcal{N} \to \mathcal{P}$ and hinders the opposite transition.

Henceforth we will denote by c the free calcium concentration, and by $n(\xi, \eta)$ the number of permissive states among $\xi \in \mathcal{S}$ and $\eta \in \mathcal{S}$. The transition rate of the i-th MH from a generic state $\beta \in \mathcal{S}$ to the state $\alpha \in \mathcal{S} \setminus \{\beta\}$, knowing that the two adjacent heads are in the states $\xi \in \mathcal{S}$ and $\eta \in \mathcal{S}$ respectively, is represented by:

$$A_{\alpha\beta}\left(c, SL, i, n(\xi, \eta)\right) . \tag{1}$$

By identifying the states $0\mathcal{N}$, $1\mathcal{N}$, $1\mathcal{P}$, $0\mathcal{P}$ with the indexes 1,2,3 and 4 respectively, the transition rates $A_{\alpha\beta}$, illustrated in Figure 3, are given as the entries of the matrix $A = (A_{\alpha\beta})$, $1 \le \alpha, \beta \le 4$:

$$A\left(c, SL, i, n\right) = \begin{bmatrix} 0 & K_{off} & 0 & \gamma^{-n} K_{pn0} \\ \bar{K}_{on}(SL,i)c & 0 & \gamma^{-n} K_{pn1} & 0 \\ 0 & \gamma^n \bar{K}_{np1}(SL,i) & 0 & \bar{K}'_{on}(SL,i)c \\ \gamma^n \bar{K}_{np0}(SL,i) & 0 & K'_{off} & 0 \end{bmatrix} .$$

In the following, we provide formulae for the involved quantities. The values of the constants are reported in Table 2.

$$\begin{aligned} \bar{K}_{np0}(SL,i) &= \chi_{LA}(SL,i)\chi_{RA}(SL,i)K_{np0}, \\ \bar{K}_{on}(SL,i) &= \chi_{RA}(SL,i)K_{on}, \end{aligned}$$

Parameter	Value	Units	Parameter	Value	Units
Sarcomere geometry			**Transition rates permissivity**		
LA (length of AF)	1.2	μm	Q_0	3	$-$
LM (length of MF)	1.65	μm	SL_Q	1.2	μm
LH (length of H-zone)	0.1	μm	α_Q	1.4	μm^{-1}
N (number of MHs)	36	$-$	K_{basic}	10	s^{-1}
Transition rates Ca binding			μ	10	$-$
K_{on}	80	$\mu M^{-1}s^{-1}$	γ	40	$-$
K_{off}	80	s^{-1}	**SL dependence**		
K'_{on}	80	$\mu M^{-1}s^{-1}$	a_R	0.1	μm
K'_{off}	8	s^{-1}	a_L	0.1	μm

Table 2: Model parameters; values taken from Washio et al. 2012.

$$\bar{K}_{np1}(SL,i) = \chi_{LA}(SL,i)\chi_{RA}(SL,i)K_{np1},$$
$$\bar{K}'_{on}(SL,i) = \chi_{RA}(SL,i)K'_{on};$$

$$x_{AZ} = (SL - LH)/2, \qquad x_{LA} = LA - x_{AZ} - LH,$$
$$x_{RA} = x_{AZ} - LA, \qquad x_i = \frac{(LM - LH)}{2\,N} i;$$

$$\chi_{RA}(SL,i) = \begin{cases} \exp\left(-\frac{(x_{RA}-x_i)^2}{a_R^2}\right) & x_i \le x_{RA} \\ 1 & x_{RA} < x_i < x_{AZ} \\ \exp\left(-\frac{(x_i-x_{AZ})^2}{a_R^2}\right) & x_i \ge x_{AZ}, \end{cases}$$
$$\chi_{LA}(SL,i) = \begin{cases} \exp\left(-\frac{(x_{LA}-x_i)^2}{a_R^2}\right) & x_i \le x_{LA} \\ 1 & x_i > x_{LA}, \end{cases}$$
$$Q(SL) = \begin{cases} Q_0 & SL \ge SL_Q \\ Q_0 - \alpha_Q(SL_Q - SL) & SL < SL_Q; \end{cases}$$

$$K_{np0} = QK_{basic}/\mu, \qquad K_{np1} = QK_{basic},$$
$$K_{pn0} = K_{basic}\gamma^2, \qquad K_{pn1} = K_{basic}\gamma^2,$$
$$K'_{on} = K_{on}, \qquad K'_{off} = K_{off}/\mu\,.$$

Following Rice et al. 2003 we assume that, when the fraction of MHs in permissive state is equal to 1, all XBs can cycle, leading to the maximum amount of generated force (the normalized force equals 1). On the other hand, when none of the MHs is in a permissive state (i.e. all MHs are in state $\mathcal{N}$), the active force cannot be generated, since XBs cannot cycle. For the intermediate levels of permissivity the amount of generated force is assumed to be proportional to the fraction of permissive heads, since each cycling XB is assumed to produce a fixed amount of force. Therefore,

denoting by $P(t)$ the permissivity (i.e. fraction of MHs in permissive state) at time t and by $F_A(t)$ the active force, we have a law of the following type:

$$F_A(t) = \alpha P(t)\,, \tag{2}$$

where α is the maximum exerted force.

2.2 Model discussion

We point out that in the model of Washio et al. 2012 the calcium-driven regulatory mechanism is associated with the MHs, rather than with the RUs, the latter being actually responsible for such mechanism (Bers 2001). In the original paper Washio et al. 2012 this association is motivated by the fact that the spacing between two consecutive MHs is similar to the one between two consecutive RUs (about 43 nm and 38 nm respectively, see e.g. Bers 2001; Keener and Sneyd 2009). Moreover, the model does not encode the description of the states of both filaments, but just of a single one; therefore, there is no need to track which unit on the one filament faces which unit on the other. The unique effect of filaments sliding which directly affects the model is the modification of the overlap region. Nevertheless, when the filaments mutually slide, the length of the overlap region is the same either if viewed from one filament or from the other.

The above considerations suggest that the modelling choice made in Washio et al. 2012 should yield just a small modelling error. Nevertheless, this modelling choice is not formally correct, thus a careful validation of the experimental results is needed. However, an extensive validation of the original model, because of the large computational cost of the MC method (more than three days to simulate a single heart beat a single core Intel i7-65000U laptop), would be unaffordable, and would be out of the scope of the present paper. Therefore, by exploiting the large reduction of computational cost of our reduced model, which allows to reduce the computational time by more than 10 000 times, we compare experimental data with the results of our model by repeating the tests made in Washio et al. 2012 and by exploring additional experimental settings.

2.3 Forward Kolmogorov Equation

From a mathematical viewpoint, the model described in Section 2.1 consists in a continuous-time Markov Chain (CTMC), or Markov Jump process, on the state space $\mathcal{S}^N$, being N the number of MHs. This model is not time-homogeneous since the transition rates may depend on time (indeed both $c(t)$ and $SL(t)$ are functions of time). Let $X_t^i \in \mathcal{S}$ be the random process associated with the i-th head. In the rest of the paper, we will use the following compact notation to denote events at time t:

$$\begin{aligned}
&(\alpha_1, \alpha_2, \ldots, \alpha_N)^t := \{X_t^1 = \alpha_1, \ldots, X_t^N = \alpha_N\}\,,\\
&(\alpha, \overset{i}{\beta}, \delta)^t := \{X_t^{i-1} = \alpha, X_t^i = \beta, X_t^{i+1} = \delta\}\,,\\
&(\alpha, \overset{i}{\beta})^t := \{X_t^{i-1} = \alpha, X_t^i = \beta\}\,,\\
&(\alpha, \beta, \overset{i}{\delta}, \eta)^t := \{X_t^{i-2} = \alpha, X_t^{i-1} = \beta, X_t^i = \delta, X_t^{i+1} = \eta\}
\end{aligned}$$

and so on. We notice that in the first definition the MH index superscript i is not necessary since the states of all the N heads are assigned.

The transition rates of Eq. (1) should be interpreted as follows: by multiplying the rates by an infinitesimal time step we get a first order approximation of the probability af a single MH to change state in the time interval $[t, t + \Delta t]$. In symbols, for each $\eta \neq \alpha_i$, we have:

$$\begin{aligned} &\mathbb{P}\left((\alpha_1, \ldots, \alpha_{i-1}, \eta, \alpha_{i+1}, \ldots, \alpha_N)^{t+\Delta t} | (\alpha_1, \ldots, \alpha_N)^t\right) \\ &= \Delta t \, A_{\eta\alpha_i}\left(c(t), SL(t), i, n(\alpha_{i-1}, \alpha_{i+1})\right) + \mathcal{O}\left(\Delta t^2\right) , \end{aligned} \tag{3}$$

where $\mathbb{P}(Z|W) = \mathbb{P}(Z \cap W)/\mathbb{P}(W)$ denotes the conditional probability of the event Z given W. On the other hand, transitions of two or more heads in any interval $[t, t+\Delta t]$ are quantities of second order in Δt. For instance, for any $\eta \neq \alpha_i$ and $\xi \neq \alpha_j$:

$$\mathbb{P}\left((\alpha_1, \ldots, \eta, \ldots, \xi, \ldots, \alpha_N)^{t+\Delta t} | (\alpha_1, \ldots, \alpha_i, \ldots, \alpha_j, \ldots, \alpha_N)^t\right) = \mathcal{O}\left(\Delta t^2\right) . \tag{4}$$

Equations (3) and (4) allow to derive the FKE for the CTMC. We have: Moreover, we have:

$$\begin{aligned} &\mathbb{P}\left((\alpha_1, \ldots, \alpha_N)^{t+\Delta t} | (\alpha_1, \ldots, \alpha_N)^t\right) \\ &= 1 - \sum_{i=1}^{N} \sum_{\xi \in \mathcal{S} \setminus \{\alpha_i\}} \mathbb{P}\left((\alpha_1, \ldots, \alpha_{i-1}, \xi, \alpha_{i+1}, \ldots, \alpha_N)^{t+\Delta t} | (\alpha_1, \ldots, \alpha_N)^t\right) + \mathcal{O}\left(\Delta t^2\right) . \end{aligned}$$

Therefore, by assembling the probabilities associated with the $N_{\text{full}} = 4^N$ possible states in a vector $\mathbf{p}(t) \in [0,1]^{N_{\text{full}}}$, one can write the evolution of the probability distribution according to the law:

$$\mathbf{p}(t + \Delta t) = \mathbf{p}(t) + \Delta t \, \mathbb{A}\mathbf{p}(t) + \mathcal{O}\left(\Delta t^2\right) ,$$

where $\mathbb{A}$ is a $N_{\text{full}} \times N_{\text{full}}$ matrix, as Eq. (**??**) is linear in each entry of $\mathbf{p}$. By taking the limit for $\Delta t \to 0$, one gets the following linear system of ODEs (FKE):

$$\dot{\mathbf{p}}(t) = \mathbb{A}\mathbf{p}(t) . \tag{5}$$

3 A reduced ODE model for sarcomere dynamics

Equation (5) provides a way to compute the exact evolution of the probability of each of the 4^N states. However, the practical resolution of this equation is infeasible because of the huge number of degrees of freedom: for $N = 36$ MHs we have $4^N \simeq 5 \cdot 10^{21}$ degrees of freedom, therefore, to represent each entry of the vector $\mathbf{p}(t)$ with 8-bytes precision, more than 37 billions of terabytes would be required just to store the vector.

However, we are not interested in the joint probability of the states of the N heads, but rather in the expected value of the number of MHs in permissive states (see Eq. (2)). Therefore, instead of studying the evolution of the probabilities of each elementary event in the state space, we look for a smaller set of events, still capable of providing an expression for the permissivity $P(t)$. Then, we look for an equation for the evolution of the probabilities associated with such events.

3.1 Assumptions and derivation

Since the transition rates of the i-th head are fully determined by the states of the triplet centred in i, it is reasonable to assume that the set of all the joint probabilities of triplets of consecutive MHs provides an effective portrait of the state of the whole system. Therefore, we consider events of the kind:

$$(\alpha, \overset{i}{\beta}, \delta)^t \quad \text{with } i = 2, \dots, N-1 \text{ and } \alpha, \beta, \delta \in \mathcal{S}. \tag{6}$$

We notice that this set of events allows to compute the permissivity (i.e. the fraction of MHs in permissive state) as follows:

$$\begin{aligned} P(t) &= \frac{1}{N} \sum_{i=1}^{N} \mathbb{P}\left(X_t^i \in \{0\mathcal{P}, 1\mathcal{P}\}\right) \\ &= \frac{1}{N} \sum_{\alpha,\delta \in \mathcal{S},\, \beta \in \{0\mathcal{P},1\mathcal{P}\}} \left[\mathbb{P}((\beta, \overset{2}{\alpha}, \delta)^t) + \sum_{i=2}^{N-1} \mathbb{P}((\alpha, \overset{i}{\beta}, \delta)^t) + \mathbb{P}((\alpha, \overset{N-1}{\delta}, \beta)^t) \right] . \end{aligned} \tag{7}$$

The time evolution of the probability of such events is given by the following relation, holding for all $i = 2, \dots, N-1$:

$$\begin{aligned} \mathbb{P}((\alpha, \overset{i}{\beta}, \delta)^{t+\Delta t}) = {} & \mathbb{P}((\alpha, \overset{i}{\beta}, \delta)^{t+\Delta t} | (\alpha, \overset{i}{\beta}, \delta)^t)\, \mathbb{P}((\alpha, \overset{i}{\beta}, \delta)^t) \\ & + \sum_{\eta \in \mathcal{S} \setminus \{\alpha\}} \mathbb{P}((\alpha, \overset{i}{\beta}, \delta)^{t+\Delta t} | (\eta, \overset{i}{\beta}, \delta)^t)\, \mathbb{P}((\eta, \overset{i}{\beta}, \delta)^t) \\ & + \sum_{\eta \in \mathcal{S} \setminus \{\beta\}} \mathbb{P}((\alpha, \overset{i}{\beta}, \delta)^{t+\Delta t} | (\alpha, \overset{i}{\eta}, \delta)^t)\, \mathbb{P}((\alpha, \overset{i}{\eta}, \delta)^t) \\ & + \sum_{\eta \in \mathcal{S} \setminus \{\delta\}} \mathbb{P}((\alpha, \overset{i}{\beta}, \delta)^{t+\Delta t} | (\alpha, \overset{i}{\beta}, \eta)^t)\, \mathbb{P}((\alpha, \overset{i}{\beta}, \eta)^t) \\ & + \mathcal{O}\left(\Delta t^2\right) . \end{aligned} \tag{8}$$

Remark 1. If the condition W has null probability, then the conditional probability $\mathbb{P}(Z|W)$ is not even defined. Nevertheless, in Eq. (8), the conditional probabilities are always multiplied by the probability of the conditions; therefore, if the event W has null probability, then the contribution of the term $\mathbb{P}(Z|W)\,\mathbb{P}(W)$ should be interpreted as zero. We will extensively adopt this convention in the following.

We now show how the conditional probabilities in Eq. (8) can be evaluated. The probability of transition of the central MH of the triplet is given, by definition of transition rate, by the following formula, where $i = 2, \dots, N-1$ and $\eta \neq \beta$:

$$\mathbb{P}((\alpha, \overset{i}{\beta}, \delta)^{t+\Delta t} | (\alpha, \overset{i}{\eta}, \delta)^t) = \Delta t A_{\beta\eta}\left(c(t), SL(t), i, n(\alpha, \delta)\right) + \mathcal{O}\left(\Delta t^2\right) .$$

On the other hand, the probability of transition of the outer MHs of the triplet cannot be computed as a function of probabilities of events in the form of (6). However, this can be computed as follows ($i = 3, \dots, N-1$ and $\eta \neq \alpha$):

$$\mathbb{P}((\alpha, \overset{i}{\beta}, \delta)^{t+\Delta t} | (\eta, \overset{i}{\beta}, \delta)^t)$$

$$
\begin{aligned}
&= \frac{\mathbb{P}((\alpha, \overset{i}{\beta}, \delta)^{t+\Delta t} \cap (\eta, \overset{i}{\beta}, \delta)^t)}{\mathbb{P}((\eta, \overset{i}{\beta}, \delta)^t)} \\
&= \frac{\sum_{\xi \in \mathcal{S}} \mathbb{P}((\xi, \alpha, \overset{i}{\beta}, \delta)^{t+\Delta t} \cap (\xi, \eta, \overset{i}{\beta}, \delta)^t)}{\mathbb{P}((\eta, \overset{i}{\beta}, \delta)^t)} + \mathcal{O}\left(\Delta t^2\right) \\
&= \frac{\sum_{\xi \in \mathcal{S}} \mathbb{P}((\xi, \alpha, \overset{i}{\beta}, \delta)^{t+\Delta t} | (\xi, \eta, \overset{i}{\beta}, \delta)^t) \, \mathbb{P}((\xi, \eta, \overset{i}{\beta}, \delta)^t)}{\mathbb{P}((\eta, \overset{i}{\beta}, \delta)^t)} + \mathcal{O}\left(\Delta t^2\right) \\
&= \frac{\sum_{\xi \in \mathcal{S}} \mathbb{P}((\xi, \alpha, \overset{i}{\beta})^{t+\Delta t} | (\xi, \eta, \overset{i}{\beta})^t) \, \mathbb{P}((\overset{i+1}{\delta})^t | (\xi, \eta, \overset{i}{\beta})^t) \, \mathbb{P}((\xi, \eta, \overset{i}{\beta})^t)}{\mathbb{P}((\eta, \overset{i}{\beta}, \delta)^t)} + \mathcal{O}\left(\Delta t^2\right) .
\end{aligned}
$$

At this stage, we make the following assumption:

$$
\mathbb{P}((\overset{i}{\delta})^t | (\xi, \eta, \overset{i-1}{\beta})^t) \simeq \mathbb{P}((\overset{i}{\delta})^t | (\eta, \overset{i-1}{\beta})^t) . \tag{9}
$$

This is equivalent to assume that the knowledge of the $(i-3)$-th MH does not provide any additional information about the probability distribution of the i-th head beyond the knowledge of the state of the $(i-1)$-th and the $(i-2)$-th head. We will return again to this concept later in Section 3.3

Using assumption (9), the calculation leads to the following result:

$$
\begin{aligned}
&\mathbb{P}((\alpha, \overset{i}{\beta}, \delta)^{t+\Delta t} | (\eta, \overset{i}{\beta}, \delta)^t) \\
&\quad \simeq \frac{\sum_{\xi \in \mathcal{S}} \mathbb{P}((\xi, \alpha, \overset{i}{\beta})^{t+\Delta t} | (\xi, \eta, \overset{i}{\beta})^t) \, \mathbb{P}((\overset{i+1}{\delta})^t | (\eta, \overset{i}{\beta})^t) \, \mathbb{P}((\xi, \eta, \overset{i}{\beta})^t)}{\mathbb{P}((\eta, \overset{i}{\beta}, \delta)^t)} + \mathcal{O}\left(\Delta t^2\right) \\
&\quad = \frac{\sum_{\xi \in \mathcal{S}} \mathbb{P}((\xi, \alpha, \overset{i}{\beta})^{t+\Delta t} | (\xi, \eta, \overset{i}{\beta})^t) \, \mathbb{P}((\xi, \eta, \overset{i}{\beta})^t)}{\mathbb{P}((\eta, \overset{i}{\beta})^t)} + \mathcal{O}\left(\Delta t^2\right) \\
&\quad = \frac{\sum_{\xi \in \mathcal{S}} A_{\alpha\eta}\left(c(t), SL(t), i-1, n(\xi, \beta)\right) \, \mathbb{P}((\xi, \overset{i-1}{\eta}, \beta)^t)}{\sum_{\xi \in \mathcal{S}} \mathbb{P}((\xi, \overset{i-1}{\eta}, \beta)^t)} \Delta t + \mathcal{O}\left(\Delta t^2\right) .
\end{aligned} \tag{10}
$$

Remark 2. The same result (10) can be equivalently obtained by proceeding as follows:

$$
\begin{aligned}
&\mathbb{P}((\alpha, \overset{i}{\beta}, \delta)^{t+\Delta t} | (\eta, \overset{i}{\beta}, \delta)^t) \\
&= \mathbb{P}((\alpha, \overset{i}{\beta})^{t+\Delta t} | (\eta, \overset{i}{\beta}, \delta)^t) + \mathcal{O}\left(\Delta t^2\right) \\
&\simeq \mathbb{P}((\alpha, \overset{i}{\beta})^{t+\Delta t} | (\eta, \overset{i}{\beta})^t) + \mathcal{O}\left(\Delta t^2\right) \\
&= \frac{\mathbb{P}((\alpha, \overset{i}{\beta})^{t+\Delta t} \cap (\eta, \overset{i}{\beta})^t)}{\mathbb{P}((\eta, \overset{i}{\beta})^t)} + \mathcal{O}\left(\Delta t^2\right) \\
&= \frac{\sum_{\xi \in \mathcal{S}} \mathbb{P}((\xi, \alpha, \overset{i}{\beta})^{t+\Delta t} \cap (\xi, \eta, \overset{i}{\beta})^t)}{\sum_{\xi \in \mathcal{S}} \mathbb{P}((\xi, \eta, \overset{i}{\beta})^t)} + \mathcal{O}\left(\Delta t^2\right)
\end{aligned}
$$

$$= \frac{\sum_{\xi\in\mathcal{S}} \mathbb{P}((\xi, \overset{i-1}{\alpha}, \beta)^{t+\Delta t} | (\xi, \overset{i-1}{\eta}, \beta)^t)\, \mathbb{P}((\xi, \overset{i-1}{\eta}, \beta)^t)}{\sum_{\xi\in\mathcal{S}} \mathbb{P}((\xi, \overset{i-1}{\eta}, \beta)^t)} + \mathcal{O}\left(\Delta t^2\right) .$$

Here we made the approximation that the transition rate of the $(i-1)$-th head does not depend on the state of the $(i+1)$-th one. However, we are neglecting the fact that the knowledge of the $(i+1)$-th head may provide information about the state of the $(i-2)$-th head, and in turn on the transition rate of the $(i-1)$-th head. This approximation is coherent with assumption (9).

With similar arguments, the following formula for the transition probability of the right MH of the triplet is recovered for $i = 2, \dots, N-2$ and $\eta \neq \delta$:

$$\mathbb{P}((\alpha, \overset{i}{\beta}, \delta)^{t+\Delta t} | (\alpha, \overset{i}{\beta}, \eta)^t) \simeq \frac{\sum_{\xi\in\mathcal{S}} A_{\delta\eta}\left(c(t), SL(t), i+1, n(\beta, \xi)\right) \mathbb{P}((\beta, \overset{i+1}{\eta}, \xi)^t)}{\sum_{\xi\in\mathcal{S}} \mathbb{P}((\beta, \overset{i+1}{\eta}, \xi)^t)} \Delta t + \mathcal{O}\left(\Delta t^2\right) .$$

The probabilities of transition of the outer MHs of the first and last triplets, on the other hand, are exactly determined as:

$$\mathbb{P}((\overset{1}{\alpha}, \beta, \delta)^{t+\Delta t} | (\overset{1}{\eta}, \beta, \delta)^t) = \Delta t\, A_{\alpha\eta}\left(c(t), SL(t), 1, n(0\mathcal{N}, \beta)\right) + \mathcal{O}\left(\Delta t^2\right) ,$$
$$\mathbb{P}((\alpha, \beta, \overset{N}{\delta})^{t+\Delta t} | (\alpha, \beta, \overset{N}{\eta})^t) = \Delta t\, A_{\delta\eta}\left(c(t), SL(t), N, n(\beta, 0\mathcal{N})\right) + \mathcal{O}\left(\Delta t^2\right) .$$

Finally, we calculate the probability that a triplet does not change state in the time interval $(t, t+\Delta t)$. We have for $i = 2, \dots, N-1$:

$$\begin{aligned}\mathbb{P}((\alpha, \overset{i}{\beta}, \delta)^{t+\Delta t} | (\alpha, \overset{i}{\beta}, \delta)^t) = 1 &- \sum_{\eta\in\mathcal{S}\setminus\{\alpha\}} \mathbb{P}((\eta, \overset{i}{\beta}, \delta)^{t+\Delta t} | (\alpha, \overset{i}{\beta}, \delta)^t) \\ &- \sum_{\eta\in\mathcal{S}\setminus\{\beta\}} \mathbb{P}((\alpha, \overset{i}{\eta}, \delta)^{t+\Delta t} | (\alpha, \overset{i}{\beta}, \delta)^t) \\ &- \sum_{\eta\in\mathcal{S}\setminus\{\delta\}} \mathbb{P}((\alpha, \overset{i}{\beta}, \eta)^{t+\Delta t} | (\alpha, \overset{i}{\beta}, \delta)^t) + \mathcal{O}\left(\Delta t^2\right) ,\end{aligned}$$

where each term have been previously calculated.

To sum up, we obtain the following nonlinear system of ODEs, for $i = 2, \dots, N-1$ (notice that $i = 1$ and $i = N$ are not comprised since no triplet is centred in the outer MHs):

$$\begin{aligned}\frac{d}{dt}\mathbb{P}((\alpha, \overset{i}{\beta}, \delta)^t) = &\sum_{\eta\in\mathcal{S}\setminus\{\alpha\}} \left[\Phi^i_L(\eta, \beta, \delta; \alpha; t) - \Phi^i_L(\alpha, \beta, \delta; \eta; t)\right] \\ &+ \sum_{\eta\in\mathcal{S}\setminus\{\beta\}} \left[\Phi^i_C(\alpha, \eta, \delta; \beta; t) - \Phi^i_C(\alpha, \beta, \delta; \eta; t)\right] \\ &+ \sum_{\eta\in\mathcal{S}\setminus\{\delta\}} \left[\Phi^i_R(\alpha, \beta, \eta; \delta; t) - \Phi^i_R(\alpha, \beta, \delta; \eta; t)\right] ,\end{aligned} \tag{11}$$

endowed with initial conditions, where we defined the probability fluxes:

$$\Phi^i_C(\alpha, \beta, \delta; \eta; t) = A_{\eta\beta}\left(c(t), SL(t), i, n(\alpha, \delta)\right) \mathbb{P}((\alpha, \overset{i}{\beta}, \delta)^t) \qquad i = 2, \dots, N-1 , \tag{12}$$

$$\Phi_L^i(\alpha,\beta,\delta;\eta;t) = \begin{cases} \frac{\left(\sum_{\xi\in\mathcal{S}} \Phi_C^{i-1}(\xi,\alpha,\beta;\eta;t)\right)\mathbb{P}((\alpha,\overset{i}{\beta},\delta)^t)}{\sum_{\xi\in\mathcal{S}}\mathbb{P}((\xi,\overset{i-1}{\alpha},\beta)^t)} & i=3,\dots,N-1 \\ A_{\alpha\eta}\left(c(t),SL(t),1,n(0\mathcal{N},\beta)\right)\mathbb{P}((\alpha,\overset{i}{\beta},\delta)^t) & i=2\,, \end{cases} \tag{13}$$

$$\Phi_R^i(\alpha,\beta,\delta;\eta;t) = \begin{cases} \frac{\left(\sum_{\xi\in\mathcal{S}} \Phi_C^{i+1}(\beta,\delta,\xi;\eta;t)\right)\mathbb{P}((\alpha,\overset{i}{\beta},\delta)^t)}{\sum_{\xi\in\mathcal{S}}\mathbb{P}((\beta,\overset{i+1}{\delta},\xi)^t)} & i=2,\dots,N-2 \\ A_{\delta\eta}\left(c(t),SL(t),N,n(\beta,0\mathcal{N})\right)\mathbb{P}((\alpha,\overset{i}{\beta},\delta)^t) & i=N-1\,. \end{cases} \tag{14}$$

We notice that when the rates in the definitions of Φ_L and Φ_R turn out to be $\frac{0}{0}$, these are set by convention equal to 0, according to Remark 1.

We notice that Eq. (11), henceforth referred to as *reduced ODE model*, is a non-linear system of ODEs while Eq. (5) is linear. However the pay-off is that the size of the system is dramatically reduced, as we switch from the $4^N \simeq 5\cdot 10^{21}$ dofs of the full model (5) to the $(N-2)\cdot 4^3 = 2176$ dofs of the reduced model (11).

3.2 Analysis of the continuous model

It easily follows that the right-hand side of Eq. (11) is globally Lipschitz continuous with respect to its argument $\mathbb{P}((\alpha,\overset{i}{\beta},\delta)^t)$. Therefore, if $c(t)$ and $SL(t)$ are uniformly bounded in the time interval $[0,T]$, then Eq. (11) admits a unique solution in the interval $[0,T]$ (see e.g. Amann 1990).

Since the unknowns of Eq. (11) are probabilities of events which are mutually related, we expect that some self-consistency conditions should hold. That is to say, we expect that the dynamics of the system is restricted to a subset of the space $[0,1]^{(N-2)\cdot 4^3}$, as it is clarified by the following definition.

Definition 1. *Let us consider a time instant $t\in[0,T]$. The associated collection of probabilities*

$$\Pi(t) = \left\{\mathbb{P}((\alpha,\overset{i}{\beta},\delta)^t)\right\}_{i=2,\dots,N-1}^{\alpha,\beta,\delta\in\mathcal{S}}$$

is said to be self-consistent if it fulfils the following conditions:

(a) $\displaystyle\sum_{\alpha,\beta,\delta\in\mathcal{S}} \mathbb{P}((\alpha,\overset{i}{\beta},\delta)^t) = 1$ *for all* $i=2,\dots,N-1$

(b) $\displaystyle\sum_{\beta,\delta\in\mathcal{S}} \mathbb{P}((\alpha,\overset{i}{\beta},\delta)^t) = \sum_{\xi,\beta\in\mathcal{S}} \mathbb{P}((\xi,\overset{i-1}{\alpha},\beta)^t)$ *for all* $i=3,\dots,N-1,\quad \alpha\in\mathcal{S}$

(c) $\displaystyle\sum_{\alpha,\beta\in\mathcal{S}} \mathbb{P}((\alpha,\overset{i}{\beta},\delta)^t) = \sum_{\beta,\xi\in\mathcal{S}} \mathbb{P}((\beta,\overset{i+1}{\delta},\xi)^t)$ *for all* $i=2,\dots,N-2,\quad \delta\in\mathcal{S}$

(d) $\displaystyle\sum_{\delta\in\mathcal{S}} \mathbb{P}((\alpha,\overset{i}{\beta},\delta)^t) = \sum_{\xi\in\mathcal{S}} \mathbb{P}((\xi,\overset{i-1}{\alpha},\beta)^t)$ *for all* $i=3,\dots,N-1,\quad \alpha,\beta\in\mathcal{S}$

Condition (a) states conservation of probability; conditions (b)–(c) state that the marginal probabilities of single MHs, when computed in different ways by means of the

joint probabilities of triplets, should lead to the same result; finally condition (d) states the same property about the joint probability of couples of adjacent MHs. Therefore, we expect that, provided that conditions (a)–(d) are satisfied at the initial time, self-consistency is maintained as time goes by. As a matter of fact, it is possible to prove the following Proposition (we report its proof in Appendix A).

Proposition 1. *Suppose that the initial state* $\Pi(0)$ *is self-consistent. Then the solution* $\Pi(t)$ *of Eq.* (11) *is self-consistent for any* $t > 0$.

By arguments similar to these used for the proof of Proposition 1, it is easy to show that the discretization of Eq. (11) based on the Forward Euler (FE) method preserves self-consistency as well:

Proposition 2. *Consider the Forward-Euler numerical approximation of Eq.* (11). *Suppose that the initial state* $\Pi_h(0)$ *is self-consistent. Then the approximate solution* $\Pi_h(t^n)$ *is self-consistent for any* $n \geq 1$.

3.3 Accuracy of the model

In the derivation of Eq. (11), the following assumptions were made:

$$\begin{aligned} \mathbb{P}((\overset{i}{\delta})^t|(\alpha,\beta,\overset{i-1}{\gamma})^t) &\simeq \mathbb{P}((\overset{i}{\delta})^t|(\beta,\overset{i-1}{\gamma})^t)\,, \\ \mathbb{P}((\overset{i}{\alpha})^t|(\overset{i+1}{\beta},\gamma,\delta)^t) &\simeq \mathbb{P}((\overset{i}{\alpha})^t|(\overset{i+1}{\beta},\gamma)^t)\,. \end{aligned} \tag{15}$$

As we already mentioned, hypotheses (15) can be interpreted as follows: if one is interested in the probability distribution of a single MH, the knowledge of the state of a MH at distance of three heads does not provide any information beyond that provided by the knowledge of the two intermediate MHs. A compact way to express this notion is to say that, at each time instant t, the states of MHs at distance of three heads are *conditionally independent* given the states of the two intermediate MHs, which reads in symbols (see Dawid 1979):

$$X_t^i \perp\!\!\!\perp X_t^{i+3}|(X_t^{i+1}, X_t^{i+2})\,, \tag{16}$$

for any $t > 0$, for $i = 1, \ldots, N-3$.

We notice that the assumption of conditional independence is different than pure independence: MHs at distance of three heads are not independent in fact; on the contrary these are strongly correlated (by observing MC simulations it is evident that the typical correlation length is much larger than 3). The assumption we are making is that the i-th head is correlated to the $i+3$-th head because these are correlated with the $(i+1)$-th and to the $(i+2)$-th respectively, which are correlated each other. In other words, we are supposing that the correlation of distant MHs is mediated by the states of the MHs located in-between. This is reasonable, since in this model we are assuming that the transition rates of MHs are affected only by adjacent units.

In order to assess the accuracy of the approximation, we consider a short filament (with $N = 6$ heads instead of 36), so that the solution of the full ODE model (5) can be computed. We impose the following c and SL transients:

$$\begin{aligned} c(t) &= \begin{cases} c_0 & t < t_0^c \\ c_0 + \frac{c_{max}-c_0}{\beta}\left[e^{-\frac{t-t_0^c}{\tau_1^c}} - e^{-\frac{t-t_0^c}{\tau_2^c}}\right] & t \geq t_0^c\,, \end{cases} \\ SL(t) &= SL_0\left[1 + \gamma_f^{max}\left(\max\left(0, 1 - e^{-\frac{t-t_0^{SL}}{\tau_0^{SL}}}\right) - \max\left(0, 1 - e^{-\frac{t-t_1^{SL}}{\tau_1^{SL}}}\right)\right)\right]\,, \end{aligned} \tag{17}$$

Variable	Value	Units	Variable	Value	Units
Dynamics of c			**Dynamics of SL**		
c_0	0.1	μM	SL_0	2.2	μm
c_{max}	1.1	μM	γ_f^{max}	-0.07	$-$
t_0^c	0.1	s	t_0^{SL}	0.15	s
τ_1^c	0.02	s	t_1^{SL}	0.55	s
τ_2^c	0.11	s	τ_0^{SL}	0.05	s
			τ_1^{SL}	0.02	s

Table 3: Constants associated with the dynamics of c and SL; values of the constants for c taken from Washio et al. 2012; values for SL set to reproduce a realistic SL transient.

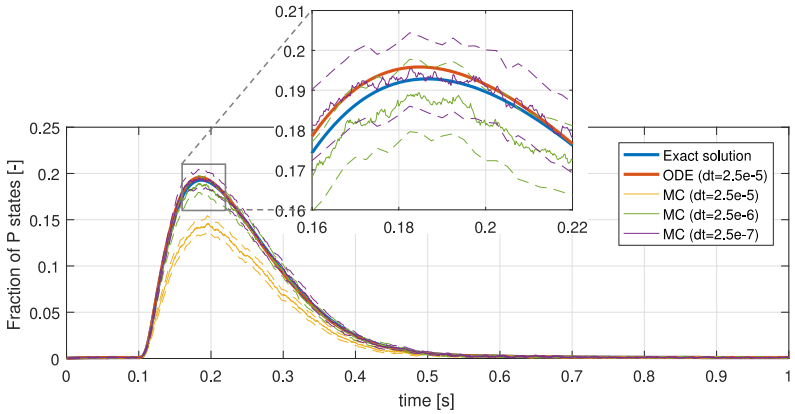

Figure 4: Comparison of the solutions for $N = 6$ of the full ODE model (5), the reduced ODE model (11), and MC simulations with different values of Δt (expressed in s). For the MC simulations the mean (solid line) and the 95% confidence intervals for the mean (dotted line) are shown. Bottom: full time interval. Top: zoom of the activation-peak.

where

$$\beta = \left(\frac{\tau_1}{\tau_2}\right)^{-\left(\frac{\tau_1}{\tau_2}-1\right)^{-1}} - \left(\frac{\tau_1}{\tau_2}\right)^{-\left(1-\frac{\tau_2}{\tau_1}\right)^{-1}}.$$

Physiological values for the constants involved in the dynamics of c and SL are reported in Table 3. Here we employ such values for the constants, with the modification $c_{max} = 5.1\,\mu M$, otherwise the "border-effect" enhanced by the shortening of the filament would lead to insignificant levels of activation.

The numerical solutions of the full ODEs system (5) and the reduced ODEs system (11) are obtained by means of the Forward Euler method, and we run a very large set of MC simulations (10^4 for each value of Δt), according to the algorithm presented in Washio et al. 2012. As suggested in the same reference, the transition rates (1) are updated at $0.25\,ms$ intervals.

Figure 4 reports a comparison of the results. For the reduced ODE model a time step of $2.5 \cdot 10^{-5}\,s$ is employed, since with larger time steps the numerical scheme may become unstable, while smaller time steps do not provide sensible improvements in

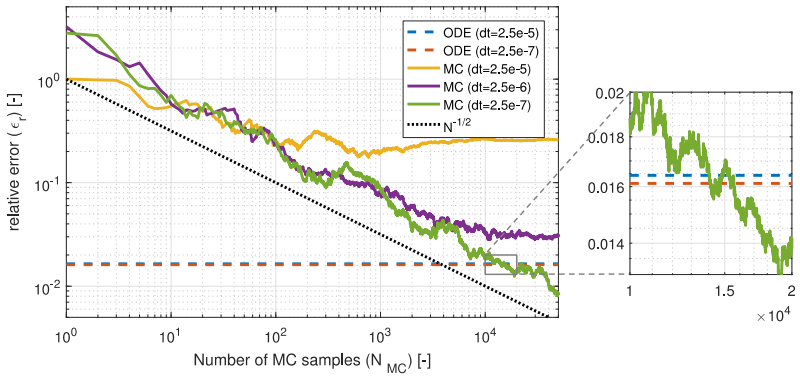

Figure 5: Relative errors in euclidean norm with respect to the results obtained through the full ODE model with $N = 6$. Right: zoom on the values of N_{MC} for which the errors obtained through MC method and the reduced ODE model are comparable.

accuracy. On the other hand, MC simulations require a much smaller time step, since the numerical solution changes significantly reducing the value of Δt.

Figure 5 compares the relative error obtained with the two methods, defined as follows. We consider a collection of time instants $\{t_1, \dots, t_{N_T}\}$, common to any time discretization of the simulations under comparison (here we consider an uniform partition of the interval 0–1 s with time step 2.5 ms). We denote by P^n_* (where $*$ stands either for ODE or MC) the numerical approximation of the exact permissivity $P(t_n)$ (which we assume to be equal to that obtained with the full ODE model (5) with $\Delta t = 1 \cdot 10^{-6} s$). The relative error in euclidean norm is defined as:

$$\varepsilon_r = \frac{\sqrt{\sum_{n=1}^{N_T} \left(P^n_* - P(t_n)\right)^2}}{\sqrt{\sum_{n=1}^{N_T} P(t_n)^2}} .$$

For the MC simulations, we consider N_{MC} random realizations of the Markov Chain, and we denote by $P^n_{MC,j}$ the random variables associated with the j-th realization. The random variables are independent and identically distributed (i.i.d.), so we can write their expected values as the sum of the exact solution and an error due to the time discretization:

$$\mathbb{E}\left[P^n_{MC,j}\right] = P(t_n) + \varepsilon^n(\Delta t), \quad \mathrm{Var}\left[P^n_{MC,j}\right] = \sigma^n(\Delta t)^2 .$$

The expected value and the variance of the MC average $P^n_{MC} = \frac{1}{N_{MC}} \sum_{j=1}^{N_{MC}} P^n_{MC,j}$ is given by:

$$\mathbb{E}\left[P^n_{MC}\right] = P(t_n) + \varepsilon^n(\Delta t), \quad \mathrm{Var}\left[P^n_{MC}\right] = \frac{\sigma^n(\Delta t)^2}{N_{MC}} .$$

Therefore, the expected value of the mean square of the errors is given by:

$$\mathbb{E}\left[\sum_{n=1}^{N_T} \left(P^n_{MC} - P(t_n)\right)^2\right] = \sum_{n=1}^{N_T} \varepsilon^n(\Delta t)^2 + \frac{\sum_{n=1}^{N_T} \sigma^n(\Delta t)^2}{N_{MC}} .$$

Thus, for relatively small values of N_{MC}, the error ε_r associated with the MC approximation is dominated by the second term and scales as $\varepsilon_r = \mathcal{O}(N_{MC}^{-1/2})$, while for

high N_{MC} the error is dominated by the term associated with the time discretization ($\varepsilon_r = \mathcal{O}(1)$ as $N_{MC} \to +\infty$).

Since the reduced ODE model (11) is an approximated model, we split the error as $\varepsilon_r = \varepsilon_r^{mod} + \varepsilon_r^{\Delta t}$, where the first term accounts for the error introduced by the model (the model error) while the second term is the contribution of the time discretization (the discretization error). For sufficiently small Δt the first term dominates over the second.

Numerical simulations were performed in Matlab and run by means of a single core Intel i7-65000U (2.50 GHz, RAM 12 GB) laptop. We notice that, in order to reach an accuracy comparable to that of the reduced ODE model, which takes 4.5 seconds for one second of physical time, at least 10^4 MC samples with $\Delta t = 2.5 \cdot 10^{-7}\, s$ are required, which takes more than 11 hours to simulate the same range of physical time. We notice that with the physiological value of MHs (i.e. $N = 36$) the gap is even more pronounced, as we switch from 15.9 seconds required by the reduced ODE model to more than 72 hours for the MC method.

3.4 Coupling with electrophysiology and mechanics

The proposed model has two input data, namely the intracellular calcium concentration $c(t)$ and the current sarcomere length $SL(t)$. The calcium concentration is an output of most current ionic models for electrophysiology (Colli Franzone, Pavarino, and Scacchi 2014; Fink et al. 2011), while the current sarcomere length can be estimated by using the rest sarcomere length SL_0 and the local deformation in the fibres direction:

$$SL(t) = SL_0 \sqrt{\mathcal{I}_{4,f}(t)}\,,$$

where $\mathcal{I}_{4,f} = \mathbf{F}\mathbf{f}_0 \cdot \mathbf{F}\mathbf{f}_0$. Here and in the following we denote by $(\mathbf{f}_0, \mathbf{s}_0, \mathbf{n}_0)$ a triplet of orthogonal vectors representing the local direction of fibres and sheets.

On the other hand, the proposed model provides as an output the fraction of permissive MHs, which in turn allows to compute the generated force in the fibres direction through Eq. (2). This allows to embed the model in either an active stress or an active strain formulation.

To provide an example, consider the active strain model proposed in Rossi et al. 2014; Ruiz-Baier et al. 2014 for contraction of the cardiac tissue. The model is based on a multiplicative decomposition of the deformation gradient ($\mathbf{F} = \mathbf{F}_E\mathbf{F}_A$), where the active component is given by

$$\mathbf{F}_A = \mathbf{I} + \gamma_f \mathbf{f}_0 \otimes \mathbf{f}_0 + \gamma_s \mathbf{s}_0 \otimes \mathbf{s}_0 + \gamma_n \mathbf{n}_0 \otimes \mathbf{n}_0\,.$$

In order to ensure that $\det(\mathbf{F}_A) = 1$ we set $\gamma_s = \gamma_n = (1+\gamma_f)^{-1/2} - 1$. By thermodynamical considerations, the following evolution law for the scalar activation function γ_f is devised, where μ_A is a viscosity parameter to be determined:

$$\mu_A \dot{\gamma_f}(t) = F_A(t) + \frac{2\mathcal{I}_{4,f}(t)}{(1+\gamma_f(t))^3} - \left.\frac{2\mathcal{I}_{4,f}}{(1+\gamma_f)^3}\right|_{c=c_0}\,.$$

By assuming that $\gamma_f = 0$ for $c = c_0$, the model reduces to the following (endowed with initial conditions):

$$\mu_A \dot{\gamma_f}(t) = F_A(t) + \frac{2\mathcal{I}_{4,f}(t)}{(1+\gamma_f(t))^3} - 2\,\mathcal{I}_{4,f}|_{c=c_0}\,,$$

where $F_A(t)$ is given by Eq. (2).

4 Numerical results

In this section, we show some numerical results obtained by the solution of the reduced ODE model (11). For the time discretization a Forward Euler scheme with a time step of $2.5 \cdot 10^{-5} s$ is employed. For computational convenience, we update the transition rates (1) at $0.25\, ms$ intervals, since they depend on quantities (SL and c) that change slowly in time. At time $t = 0$ the sarcomere is assumed to be fully deactivated, namely all MHs are in state $0\mathcal{N}$. In other words the following initial condition is applied:

$$\mathbb{P}((\alpha, \overset{i}{\beta}, \delta)^0) = \begin{cases} 1 & \text{if } \alpha = \beta = \delta = 0\mathcal{N} \\ 0 & \text{else.} \end{cases}$$

In some cases, we perform the same numerical tests also with the original model of Washio et al. 2012 by means of the MC method, and we compare the results with those of our reduced model. For all the simulations we show the results obtained with $N_{MC} = 10^4$ samples, since as shown Section 3.3 this amount of samples is required to keep fluctuations below a reasonable level. In the dynamic case, we employ a time step of $\Delta t = 2.5 \cdot 10^{-7} s$ (required to keep the discretization error under control, see Section 3.3); for the steady-state simulations instead, since we are interested just in the equilibrium configuration, we employ a time of $\Delta t = 2.5 \cdot 10^{-5} s$.

We validate the numerical results against the experimental data. With this aim, since we assume that the developed force is proportional to the level of permissivity (see Eq. (2)), we compare the experimentally measured force with the numerical permissivity, obtained by evaluating Eq. (7) on the numerical solution of the reduced ODE model (11). Since we do not have a closure law between force and permissivity, and these are assumed to be just mutually proportional, we remark that one should always compare their normalized values.

The goal of the numerical tests is twofold. First, we validate our model against the original one (Washio et al. 2012) to assess the validity of the reduction procedure shown in Section 3. Then, thanks to the large complexity reduction and negligible computational cost allowed by our model, we use it to explore additional experimental settings. The aim it to verify that the modelling choice introduced in Washio et al. 2012 and discussed in Section 2.2 does not compromise the validity of the model. Whenever experimental measurements are available, we compare our numerical results against these ones.

4.1 Steady-state

By fixing the calcium level c and the sarcomere length SL, letting the system reach the steady-state and considering the level of activation at the equilibrium, one gets the steady-state relationships between calcium and force and between length and force. The capability of reproducing the physiological steady-state curves is a distinguishing feature of activation models (see Rice and Tombe 2004 for their role).

In this section, we consider the steady-state curves obtained by solving the reduced ODE model (11) and the full model of Washio et al. 2012 and we compare them with the experimental measurements of Kentish et al. 1986 and Dobesh, Konhilas, and Tombe 2002. Both data sets refer to skinned rat cardiac trabeculae.

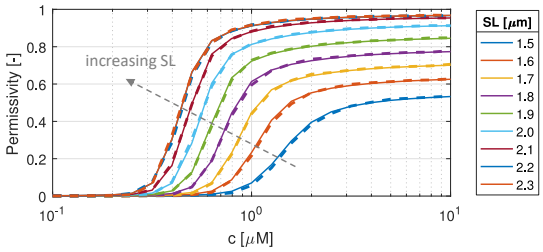

(a) Permissivity versus c: full model (dashed lines) and reduced ODE model (solid lines)

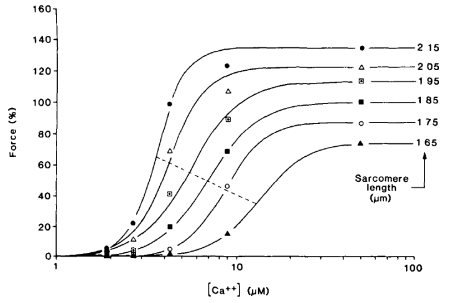

(b) Force versus c: experimental data from Kentish et al. 1986

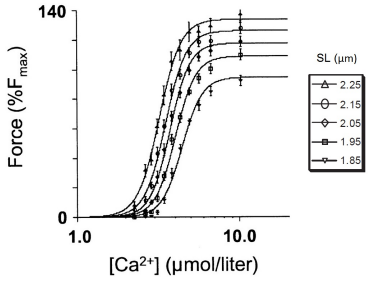

(c) Force versus c: experimental data from Dobesh, Konhilas, and Tombe 2002

Figure 6: Steady-state force-calcium relationship for different SL: comparison of the results of the reduced ODE model (a) with the results of the full model of Washio et al. 2012 (a) and with experimental curves ((b) and (c)). Notice that, since we assume that force is proportional to permissivity (see Eq. (2)), normalized permissivity can be compared with normalized force.

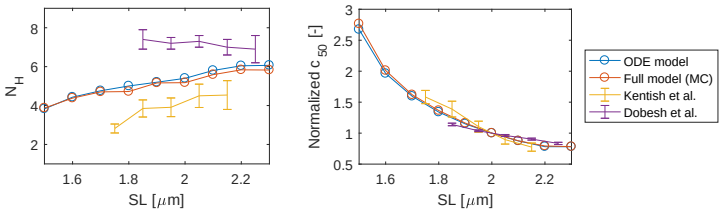

(a) N_H versus SL (b) Normalized c_{50} versus SL

Figure 7: Dependence of the Hill coefficient N_H (a) and the calcium level corresponding to half activation c_{50} (b) on the sarcomere length SL, compared with experimental data. The Hill coefficients obtained with the proposed model and the full model of Washio et al. 2012 are comprised between the two experimental sets, and have a similar trend to those on Kentish et al. 1986. Also c_{50} report a similar trend to experimental measurements. Notice that, since the skinning procedure employed in the experiments alters significantly the calcium level which triggers activation, the values of c_{50} are normalized to the value assumed at $SL = 2.0\,\mu m$.

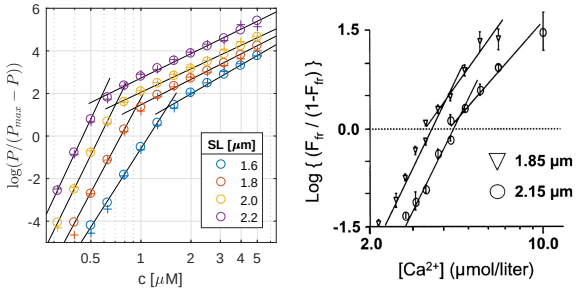

(a) Full model (+) and reduced ODE model (∘)

(b) Experimental data from Dobesh, Konhilas, and Tombe 2002

Figure 8: Steady-state force-calcium relationship in the plane $\log c$ versus $\log(F_A/(F_{max}-F_A))$, for different SL: comparison of the results of the reduced ODE model (a) with the results of the full model of Washio et al. 2012 (a) and with experimental curves (b). We notice that the quantities on the y-axis of the two plots are coincident, since $\log(P/(P_{max}-P_A)) = \log(F_A/(F_{max}-F_A)) = \log(F_{rel}/(1-F_{rel}))$, where $F_{rel} = F_A/F_{max}$. We remark that, in (b), taken from Dobesh, Konhilas, and Tombe 2002, the triangle and circle bullets are incorrectly indicated and should be switched.

4.1.1 Force-calcium relationship

Figure 6 shows the steady-state force-calcium relationship for different values of SL obtained with the proposed model, and compares them with the experimental measurements. Experimental data show that the steady-state force-calcium relationship, for a prescribed value of SL, is approximated by the sigmoidal Hill's function (see Dobesh, Konhilas, and Tombe 2002; Kentish et al. 1986):

$$F_A(c) = \frac{F_{max}}{1 + \left(\frac{c_{50}}{c}\right)^{N_H}}, \tag{18}$$

where F_{max} is the plateau force at high calcium concentrations, c_{50} is the calcium level at 50% of maximum developed force, and $N_H \geq 1$ is the so–called Hill coefficient. The Hill coefficient measures the level of cooperativity: $N_H = 1$ means no cooperativity at all; the highest the value of N_H, the steepest the force-calcium curve at c_{50}.

According to experimental observations, the effect of SL on the force-calcium relationship is threefold:

- As SL increases, in the physiological range (approximately $1.7 - 2.3\,\mu m$), the sarcomere becomes more sensitive to c. This translates into a leftward shift of the curve, or equivalently in a reduction of c_{50}. In Figure 7b the dependence of c_{50} on SL obtained by solving the reduced ODE model is compared to experimental data. Since there is evidence that the skinning procedure (i.e. the removal of the cell membrane), employed in both sets of measurement, lower the sarcomere sensisivity to calcium (Gao et al. 1994; Kentish et al. 1986; Rice, Winslow, and Hunter 1999), it is not meaningful to compare the absolute values of c_{50}; for this reason calcium concentrations are normalized.

- The dependence of the Hill coefficient N_H on SL is still under debate. Experi-

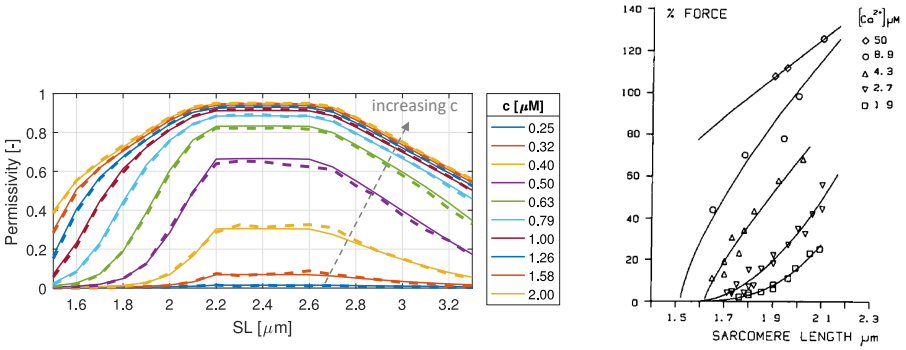

(a) Full model (dashed lines) and reduced ODE model (solid lines)

(b) Experimental data from Kentish et al. 1986

Figure 9: Steady-state force-length relationship for different calcium concentrations: comparison of the results of the reduced ODE model (a) with the results of the full model of Washio et al. 2012 (a) and with experimental curves (b), available only in the physiological range ($1.6\,\mu m \leq SL \leq 2.2\,\mu m$). Notice that the curves report the observed change in convexity (see text for details).

mental data of Dobesh show a limited dependence of cooperativity on SL, while the measurements of Kentish show a clear increase in cooperativity as the sarcomere gets longer. Our model shows a trend similar to the latter experimental observations (see Figure 7a). The level of cooperativity is intermediate between the two sets of data. Notice that also the level of cooperativity N_H may be affected by the skinning procedure (Dobrunz, Backx, and Yue 1995; Gao et al. 1994).

- The maximal force F_{max} increases as SL grows. The results obtained with the reduced ODE model exhibit this behaviour. This dependence is discussed in more details in Section 4.1.2.

We notice that it is possible to reformulate (18) into:

$$\log\left(\frac{F_A(c)}{F_{max} - F_A(c)}\right) = N_H\left(\log c - \log c_{50}\right) .$$

Therefore, for an exact Hill's function, the force-calcium relationship is a line in the plane $\log(F_A/(F_{max}-F_A))$ versus $\log c$. However, it is well known (see Rice and Tombe 2004) that in real muscles the curve can be better fitted by two distinct lines, thus showing a higher cooperativity at lower calcium levels (see Figure 8b). In Figure 8a the corresponding curves obtained with the proposed model are shown, with the best-fit lines in the least-squares sense, in comparison with experimental measurements. We notice that our model is capable of reproducing physiological features such as: (i) force-calcium relationship, which is fitted by two distinct lines, with decreasing slope as c increases; (ii) the intersection between these lines, which lies above the level of half activation (i.e. $\log(F_A/(F_{max} - F_A)) = 0$, which corresponds to $F_A = F_{max}/2$); (iii) the slopes of both lines, which are nearly independent of SL; (iv) the normalized force corresponding to the intersection between these lines, which is nearly independent of SL; (v) the calcium level corresponding to half activation, which decreases as SL increases.

In Figures 6–8 we compare the results of our reduced model with those obtained by simulating the full model of Washio et al. 2012 by means of the MC method. This comparison shows a very good qualitative and quantitative agreement between the two, and thus supports the validity of assumption (15).

4.1.2 Force-Length relationship

In Figure 9a the force-length curves of the proposed model for different calcium levels are reported. Because of the overlapping between the AFs near the H-zone, which lower the number of interacting actin and myosin units, the force exerted by a shortened sarcomere is smaller than the force of a relaxed sarcomere (corresponding to $SL \simeq 2.2\mu m$). In the range $2.2\,\mu m \leq SL \leq 2.6\,\mu m$ the whole MF faces a single AF, which is the most favourable condition for muscle activation, and the permissivity is constant. For $SL > 2.6\,\mu m$ the central region of the MF faces no AF, and the width of the region increase as SL increases, making the permissivity reduce.

We notice that the curves of Figure 9a resemble the *sarcomere overlap function* employed in mean field models to account for the effect of SL (Sachse 2004; Trayanova and Rice 2011); however, whereas in those models the force-length dependency is assumed to be invariant with respect to c, our model is capable of capturing the calcium dependency of the force-length relationship. Indeed, force-length curves obtained with our model exhibit the change in curvature observed experimentally (see Kentish et al. 1986): in the physiological range ($1.6\,\mu m \leq SL \leq 2.2\,\mu m$), the curves are convex at low calcium levels, concave at intermediate calcium levels, while at maximally activating c the relation is approximately linear (see Figure 9b). We notice that also in this case the reduced ODE model accurately reproduces the results of the full model of Washio et al. 2012 obtained by means of the MC method.

4.2 Isosarcometric versus shortening twitches

We showed in Section 3.3 that with $N = 6$ MHs our reduced model reproduces with a good qualitative and quantitative correspondence the results with the full model of Washio et al. 2012. In this Section we investigate whether this is still valid when we consider the physiological number of MHs (i.e. $N = 36$). Since the numerical solution of the full ODEs system (5) cannot be achieved because of the gigantic number of dofs ($4^N \simeq 5 \cdot 10^{21}$), we compare the results of our reduced model with those obtained by means of the MC method.

With this aim, we perform the following test, also reported in Washio et al. 2012. The calcium concentration and the sarcomere length time transients taken from Janssen and Tombe 1997 are applied, and the resulting force obtained with the reduced ODE model and with the full model of Washio et al. 2012 are compared with the experimental observations, both under isosarcometric conditions and during a shortening twitch (see Figure 10).

As mentioned before, since the generated force is taken proportional to permissivity (see section 2.1), we compare the experimentally observed force, normalized with respect to its peak during isosarcometric contraction, with the permissivity P normalized with respect to its peak under the same conditions.

Figure 10 shows a very good qualitative and quantitative agreement between the results fo the reduced ODE model and those obtained with the MC method, thus supporting the validity of our reduced model with respect to the full model.

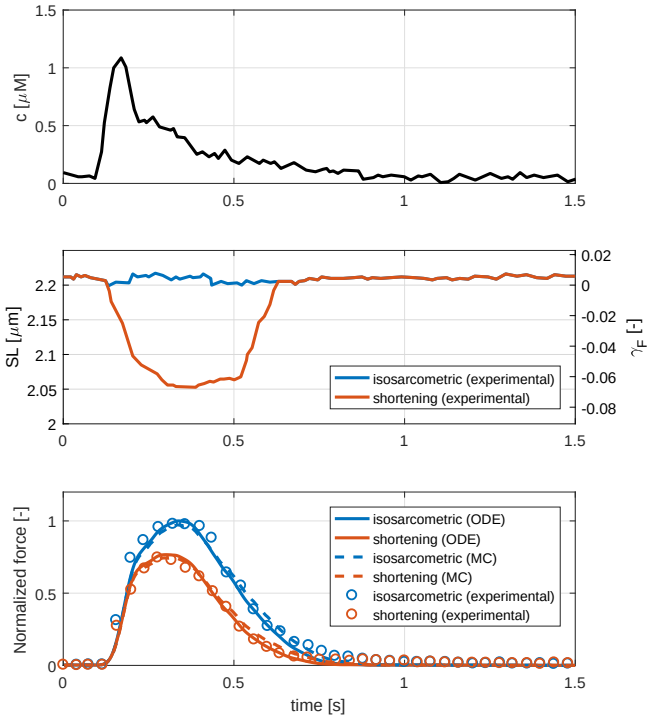

Figure 10: Time transients of calcium concentration c (top) and sarcomere length SL (middle) taken from Washio et al. 2012; normalized force (bottom) obtained with the reduced ODE model (solid lines), with the full model of Washio et al. 2012 (dashed lines) and experimentally observed (circles, taken from Washio et al. 2012).

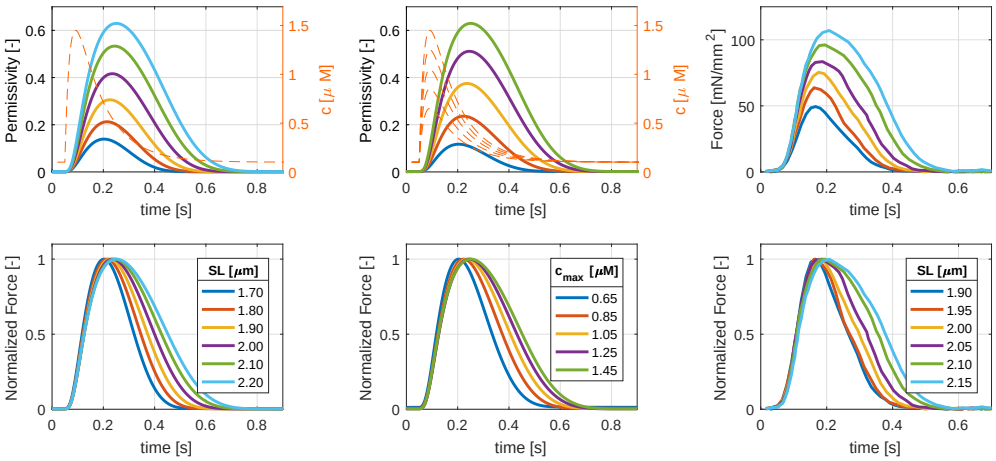

Figure 11: Force transients in isosarcometric twitch contractions, without (first line) and with (second line) normalization. First column: reduced ODE model results for $c_{max} = 1.45\,\mu M$ and different values of SL. Second column: reduced ODE model results for $SL = 2.2\,\mu m$ and different values of c_{max}. Third column: experimental measurements with fixed maximum calcium level and different SL, expressed in μm (data from Janssen and Hunter 1995). In the first two columns, solid lines refer to permissivity (axis on the left), while dashed lines refer to calcium concentration (axis on the right). In both experimental and numerical cases activation started at $0.05\,s$.

4.3 Isosarcometric twitch contractions

In Section 4.1 we have considered the stationary solutions of the proposed model. In order to test the capability of the reduced ODE model of reproducing the dynamics of the sarcomere, we simulate twitches by imposing the calcium transient of Eq. (17), while keeping the value of SL constant. We run several simulations, by changing the sarcomere length SL and the calcium concentration peak c_{max}. In Figure 11 the obtained results are compared with the experimental observations on rat trabeculae reported in Janssen and Hunter 1995.

Changes in either the sarcomere length or in the calcium peak have three distinct effects on the force transient. The same effects can be recorded either with fixed SL and increasing c_{max} (see Janssen and Hunter 1995), or by keeping c_{max} constant and increasing SL (see Dobrunz, Backx, and Yue 1995). The three effects, all exhibited by the numerical solutions of the reduced ODE model (see Figure 11), are the following:

- Increment of peak force;
- Increment of rate of force development. More specifically, the force development rate is approximately proportional to peak force, or, in other terms, the time of force development is nearly constant as SL or c_{max} vary. This observation is more evident in the normalized curves in the right column of Figure 11;
- Increment of relaxation time.

It has been experimentally observed (see Janssen and Hunter 1995; Rice et al. 2008) that the third effect, namely the slowing down of the relaxation phase, is more influenced by changes in SL than by changes in c_{max}. This feature too can be observed on the results of the proposed model. Indeed, in Figure 12 two force transients

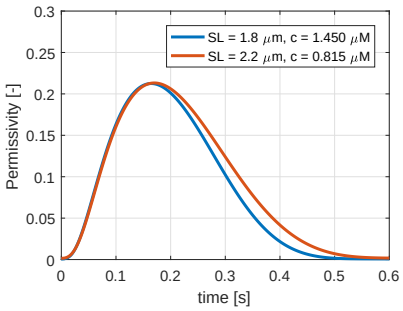

(a) Reduced ODE model

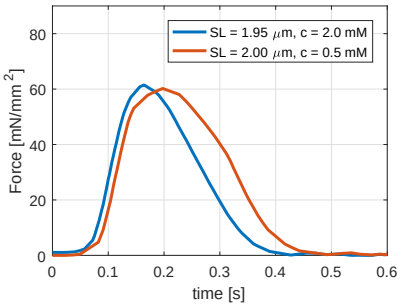

(b) Experimental data from Janssen and Hunter 1995

Figure 12: Comparison of force transients of twitches with similar peak force and different SL and c_{max}: simulations results (a) and experimental measurements (b). In both cases, the larger SL the longer the relaxation phase.

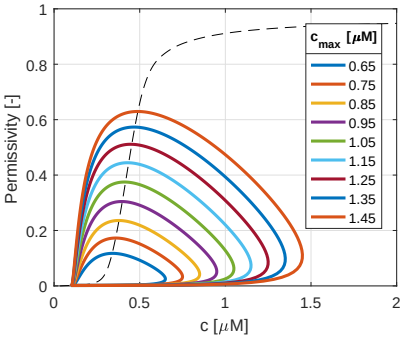

(a) Reduced ODE model

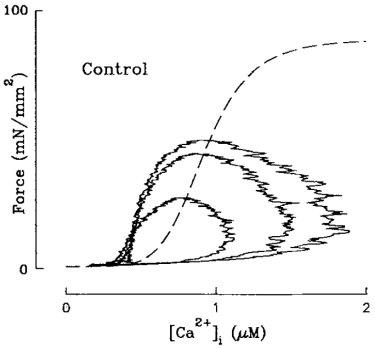

(b) Experimental data from Backx et al. 1995

Figure 13: Loops in phase diagram of twitch responses (solid lines) and steady-state force-calcium relationship (dashed line): comparison of the reduced ODE model results (a) with experimental data (b). Experimental data, taken from Backx et al. 1995 refer to intact rat cardiac trabeculae at $SL = 2.1$–$2.3\,\mu m$.

associated with two different couples (SL, c_{max}), but exhibiting a similar peak force, are compared: the relaxation time is slower in the curve associated with the larger SL.

In Figure 13 isosarcometric twitches are plotted as phase loops and compared with experimental measurements on intact rat cardiac trabeculae (Backx et al. 1995). The figure highlights the delayed response of force with respect to calcium: in the early stages of the twitches, loops are placed below the steady-state curve (dashed line), meaning that calcium has peaked while force is still low; then the trajectories cross the steady-state curve with nearly null derivative (this corresponds to the force peak), and eventually they return to their initial configuration staying above the steady-state curve.

4.4 Rate of tension development

When a sarcomere undergoes a sudden length change, the shock causes the detachment of nearly all XBs, making the tension abruptly fall to zero, and then recover the pre-existing level with an exponential-like recovery. A common experimental characterization of the muscle is through the parameter k_{tr}, namely the rate of tension redevelopment after the sudden length change (see Araujo and Walker 1994; Ford, Huxley, and Simmons 1977; Tombe and Stienen 1997).

In order to reproduce this experimental setting with the proposed model, we keep the calcium level c fixed until the steady state is reached; then, to simulate XBs detachment we force the transition from the permissive state $\mathcal{P}$ to the non-permissive state $\mathcal{N}$ for all MHs. The results, for different calcium levels, are reported in Figure 14a. The rates of tension redevelopment k_{tr} are estimated through a least-square fitting of the curves with a single exponential, and are reported in Figure 14c. In Figure 14b the tension redevelopment transients, measured in rat skinned ventricular cardiomyocytes and reported in Wolff, McDonald, and Moss 1995, are shown with their exponential fit.

The relationships between the maximal force and the rate of tension redevelopment obtained experimentally and numerically are compared in Figure 14c. The experimentally-estimated rates show good match with those obtained with the proposed model, and exhibit the same increasing trend as maximal force increases.

4.5 Coupled electromechanical model of the sarcomere

A simple zero-dimensional version of the active strain formulation described in Section 3.4 can be derived by assuming that $\mathbf{F}_E = \mathbf{I}$, which entails $\mathcal{I}_{4,f} = (1+\gamma_f)^2$. Under this hypothesis the model reduces to:

$$\mu_A \dot{\gamma_f}(t) = \alpha\, P(t) + 2\left[\frac{1}{1+\gamma_f(t)} - 1\right], \tag{19}$$

and the current sarcomere length is computed as

$$SL(t) = SL_0(1+\gamma_f(t))\,.$$

By applying the calcium transient of Eq. (17) and by coupling the reduced ODE model (11) with Eq. (19), we obtain a zero-dimensional active-passive mechanical model of cardiac contraction. We show in Figures 15 and 16 the results of numerical simulations of this simple model, with different values of μ_A and α.

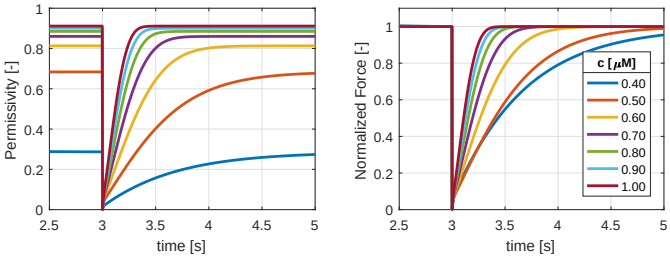

(a) Reduced ODE model

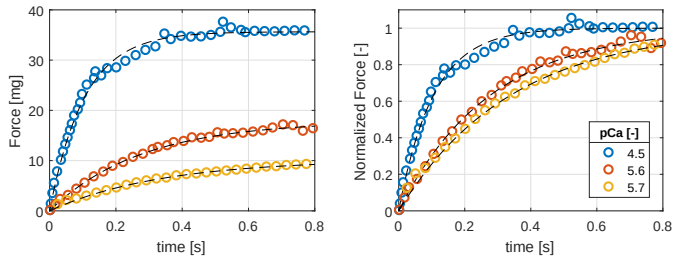

(b) Experimental data from Wolff, McDonald, and Moss 1995

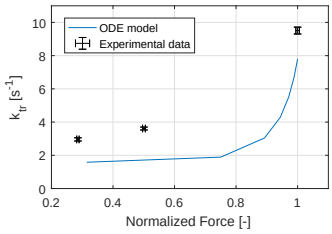

(c) Rates of tension redevelopment

Figure 14: (a): Tension redevelopment transients obtained with the ODE model for different calcium levels (left: non-normalized curves; right: normalized curves). (b) Tension redevelopment transients after sudden XBs detachment obtain with a best fit on measurements taken from Wolff, McDonald, and Moss 1995. The curves refer to different calcium levels, expressed in pCa $= -\log(c/(1\mu M))$. (c) Rate of tension redevelopment after sudden XBs detachment as function of normalized force: comparison of numerical results with experimental measurements in rat skinned ventricular cardiomyocytes taken from Wolff, McDonald, and Moss 1995, reported as least-squares fitting with standard-error (SE) bars.

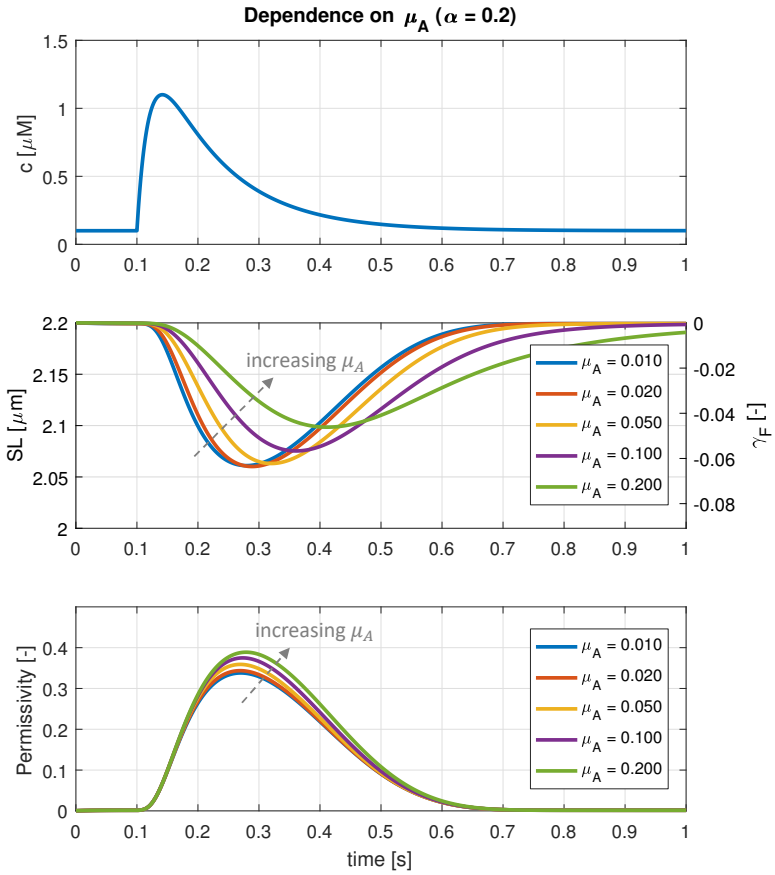

Figure 15: Time transients of calcium concentration c (top), sarcomere length SL (middle) and permissivity P (bottom) for different values of μ_A, displayed in the legend, and $\alpha = 0.2$. The applied c transient is given by Eq. (17), while SL and P are obtained by coupling the reduced ODE model (11) with (19).

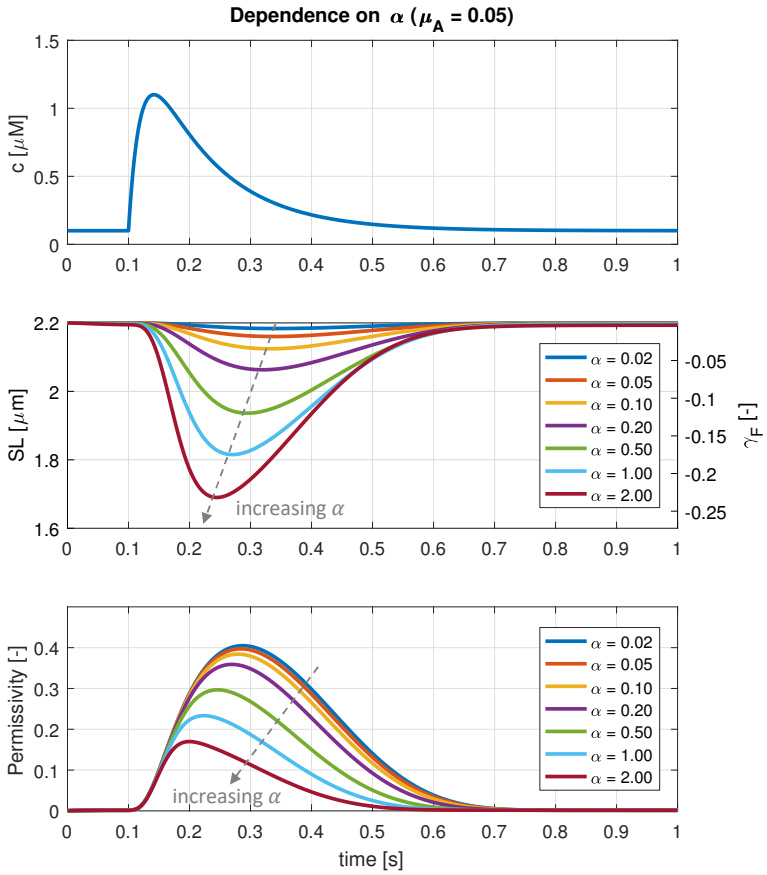

Figure 16: Time transients of calcium concentration c (top), sarcomere length SL (middle) and permissivity P (bottom) for different values of α, displayed in the legend, and $\mu_A = 0.05$. The applied c transient is given by Eq. (17), while SL and P are obtained by coupling the reduced ODE model (11) with (19).

5 Conclusions

We have developed a mathematical model based on an ODEs system suitable to approximate the Forward Kolmogorov Equation associated with the Continuous Time Markov Chain model for sarcomere contraction presented in Washio et al. 2012. The proposed model condensates the $5 \cdot 10^{21}$ variables of the original system into less than 2 200 variables. Moreover, the proposed model produces very accurate results with a much lower computational effort than the original model, whose complexity dictates the use of the MC method: the simulation of one second of physical time takes about 15.9 seconds with the reduced ODE model, against more than 72 hours required on the same computer platform by the original model.

We showed through numerical tests that the model is able to reproduce physiological behaviours observed under various experimental settings, including the steady-state relationships between calcium, length and force, isosarcometric and shortening twitches, and force redevelopment after a sudden active force drop. This supports the hypotheses on which also the original model of Washio et al. 2012 is based, as discussed in Section 2.2.

Compared with previously proposed reduction strategies, the concept proposed in this work presents significant advantages. First, it does not require the so-called "ring" approximation employed both in Rice et al. 2003 and in Campbell et al. 2010, making the model able to capture the border-effect at filament end-points. Moreover, as highlighted in Section 1, the strategy proposed in Rice et al. 2003 is limited to steady conditions, while the complexity of the reduced model of Campbell et al. 2010 is still too high to allow that more than 9 RUs are simulated. The approach proposed in Washio et al. 2012 produces a larger complexity reduction, compared to the present work, since it ends up with a system of 144 ODEs, but it still requires a time consuming off-line phase to tune the model by fitting the registered data. Moreover, the error introduced by the approximation is larger than in the present work and the validity of the parameters is not guaranteed beyond the settings used to tune them. The technique proposed in Land and Niederer 2015 yields a system of 750 ODEs, but still requiring a long off-line phase to compute transition rates. Finally, having characterized each state by the number of unblocked RUs and bound XBs, the explicit spatial description is lost during the reduction procedure. Therefore, length-dependent effects an tension are neglected and their inclusion would require modifications to the employed strategy.

We remark that our approach to complexity reduction is not limited to the current model, but it can be applied to any spatially explicit Markov Chain model with end-to-end cooperative interactions. In general, given a model comprising N units, each described by a CTMC with S states, assumption (15) yields to an ODEs system with $(N-2) \cdot S^3$ variables, in place of the S^N dofs of the original model.

As previously mentioned, unlike most previously proposed techniques, our approach does not require an off-line phase to calibrate model parameters, given sub-cellular properties. The advantage is that this property speeds up the investigation of the influence of those microscopic properties, such as changes in individual channels or proteins, on the tissue contractile properties. Moreover, it opens to the possibility of investigating dynamic changes of sub-cellular properties.

We envision, among the others, the following possible developments. The model presented in this paper can be coupled with some existing models of cardiac electrophysiology and passive mechanics, as outlined in Section 3.4 (see Gerbi, Dedè, and Quarteroni 2017). Moreover, since the original model of Washio et al. 2012 is restricted

to thin filament dynamics, it does not incorporate velocity-dependent effects, which are linked to XB dynamics (see e.g. Keener and Sneyd 2009). Therefore, we plan to enrich the present model with a more accurate description of XB cycling. This would also allow to account for the dynamics of metabolite concentrations (ATP, ADP and P_i), and thus to investigate the energy consumption of the heart as well as the effects of hypoxia on the heart beat.

Appendix A Proof of Proposition 1

In view of the proof of Proposition 1 we state the following Lemma.

Lemma 1. *Consider a function $\mathbf{\Phi}\colon \mathbb{R}^N \times [0,T] \to \mathbb{R}^N$, globally Lipschitz continuous in its first argument, uniformly w.r.t. the second. Let W be an M-by-N matrix, satisfying:*

$$\mathbf{\Phi}(\mathbf{x},t) \in \mathrm{Ker}(W) \qquad \forall\, \mathbf{x} \in \mathrm{Ker}(W), \quad t \in [0,T]\,. \tag{20}$$

Let $\mathbf{x}(t)$ be the solution of:

$$\begin{cases} \dot{\mathbf{x}}(t) = \mathbf{\Phi}(\mathbf{x}(t),t) & t \in [0,T] \\ \mathbf{x}(0) = \mathbf{x}_0 \in \mathrm{Ker}(W)\,. \end{cases} \tag{21}$$

Then, $\mathbf{x}(t) \in \mathrm{Ker}(W)$ for any $t \in [0,T]$.

Proof. Let $\{\mathbf{x}_1, \dots, \mathbf{x}_n\}$ be an orthonormal basis of the space $\mathrm{Ker}(W)$. We define the matrix $X = \begin{bmatrix} \mathbf{x}_1 & | & \cdots & | & \mathbf{x}_n \end{bmatrix}$, whose column vectors are the $\mathbf{x}_k$'s. Let $\mathbf{y}^*(t) \in \mathbb{R}^n$ be the solution of the following system:

$$\begin{cases} \dot{\mathbf{y}}(t) = X^T \mathbf{\Phi}(X\mathbf{y}(t),t) & t \in (0,T] \\ \mathbf{y}(0) = X^T \mathbf{x}_0\,. \end{cases} \tag{22}$$

Existence and uniqueness of $\mathbf{y}^*(t)$ is ensured by the fact that the map $\mathbf{y} \mapsto X^T \mathbf{\Phi}(X\mathbf{y},t)$ is globally Lipschitz continuous, uniformly w.r.t. t. Define $\mathbf{x}^*(t) = X\mathbf{y}^*(t) \in \mathrm{Ker}(W)$. We now show that $\mathbf{x}^*(t)$ is solution of Eq. (21). Indeed, we have:

$$\dot{\mathbf{x}}^*(t) = X\dot{\mathbf{y}}^*(t) = P_{\mathrm{Ker}(W)} \mathbf{\Phi}(\mathbf{x}^*(t),t) = \mathbf{\Phi}(\mathbf{x}^*(t),t)\,,$$

where $P_{\mathrm{Ker}(W)} = XX^T$ denotes the projection matrix on the subspace $\mathrm{Ker}(W)$. The last equality is due to the fact that, thanks to (20), $\mathbf{\Phi}(\mathbf{x}^*(t),t) \in \mathrm{Ker}(W)$. As to the initial datum, we have $\mathbf{x}^*(0) = P_{\mathrm{Ker}(W)}\mathbf{x}(0) = \mathbf{x}(0)$. The thesis follows thanks to the uniqueness of the solution of (21). □

We can now prove the result of Proposition 1.

Proof of Proposition 1. It is easily shown that:

$$\frac{d}{dt} \sum_{\alpha,\beta,\delta \in \mathcal{S}} \mathbb{P}((\alpha, \overset{i}{\beta}, \delta)^t) = 0 \qquad \text{for all } i = 2, \dots, N-1.$$

Therefore, if condition (a) of Definition 1 holds for $t = 0$, then it holds also for each $t > 0$.

To prove conditions (b)–(d) of Definition 1 for $t > 0$, we apply Lemma 1 (notice that conditions (b)–(d) can be written in the form $W\mathbf{x} = 0$, where $\mathbf{x}$ denotes the state $\Pi(t)$). In order to apply Lemma 1, we are left to show that (20) holds.

For this purpose, the following result will be used several times. Let us assume that the state $\Pi(t)$ satisfies condition (d). Then, for $i = 3, \ldots, N-1$:

$$\begin{aligned}
&\sum_{\delta\in\mathcal{S}}\sum_{\eta\in\mathcal{S}\setminus\{\alpha\}}\left[\Phi_L^i(\eta,\beta,\delta;\alpha;t)-\Phi_L^i(\alpha,\beta,\delta;\eta;t)\right]\\
&\quad=\sum_{\delta\in\mathcal{S}}\sum_{\eta\in\mathcal{S}\setminus\{\alpha\}}\left[\frac{\left(\sum_{\xi\in\mathcal{S}}\Phi_C^{i-1}(\xi,\eta,\beta;\alpha;t)\right)\mathbb{P}((\eta,\overset{i}{\beta},\delta)^t)}{\sum_{\xi\in\mathcal{S}}\mathbb{P}((\xi,\overset{i-1}{\eta},\beta)^t)}\right.\\
&\qquad\qquad\left.-\frac{\left(\sum_{\xi\in\mathcal{S}}\Phi_C^{i-1}(\xi,\alpha,\beta;\eta;t)\right)\mathbb{P}((\alpha,\overset{i}{\beta},\delta)^t)}{\sum_{\xi\in\mathcal{S}}\mathbb{P}((\xi,\overset{i-1}{\alpha},\beta)^t)}\right]\\
&\quad=\sum_{\eta\in\mathcal{S}\setminus\{\alpha\}}\left[\left(\sum_{\xi\in\mathcal{S}}\Phi_C^{i-1}(\xi,\eta,\beta;\alpha;t)\right)\underbrace{\frac{\sum_{\delta\in\mathcal{S}}\mathbb{P}((\eta,\overset{i}{\beta},\delta)^t)}{\sum_{\xi\in\mathcal{S}}\mathbb{P}((\xi,\overset{i-1}{\eta},\beta)^t)}}_{=1}\right.\\
&\qquad\qquad\left.-\left(\sum_{\xi\in\mathcal{S}}\Phi_C^{i-1}(\xi,\alpha,\beta;\eta;t)\right)\underbrace{\frac{\sum_{\delta\in\mathcal{S}}\mathbb{P}((\alpha,\overset{i}{\beta},\delta)^t)}{\sum_{\xi\in\mathcal{S}}\mathbb{P}((\xi,\overset{i-1}{\alpha},\beta)^t)}}_{=1}\right]\\
&\quad=\sum_{\eta\in\mathcal{S}\setminus\{\alpha\}}\sum_{\xi\in\mathcal{S}}\left[\Phi_C^{i-1}(\xi,\eta,\beta;\alpha;t)-\Phi_C^{i-1}(\xi,\alpha,\beta;\eta;t)\right]\ .
\end{aligned}$$

Similarly, we have for $i = 2, \ldots, N-2$:

$$\begin{aligned}
&\sum_{\alpha\in\mathcal{S}}\sum_{\eta\in\mathcal{S}\setminus\{\delta\}}\left[\Phi_R^i(\alpha,\beta,\eta;\delta;t)-\Phi_R^i(\alpha,\beta,\delta;\eta;t)\right]\\
&\quad=\sum_{\eta\in\mathcal{S}\setminus\{\delta\}}\sum_{\xi\in\mathcal{S}}\left[\Phi_C^{i+1}(\beta,\eta,\xi;\delta;t)-\Phi_C^{i+1}(\beta,\delta,\xi;\eta;t)\right]\ .
\end{aligned}$$

Thus, under the hypothesis that the state $\Pi(t)$ satisfies condition (d), the computation of the time derivative of both sides of (b) leads to the same result, i.e.:

$$\frac{d}{dt}\sum_{\xi,\beta\in\mathcal{S}}\mathbb{P}((\xi,\overset{i-1}{\alpha},\beta)^t)=\sum_{\eta\in\mathcal{S}\setminus\{\alpha\}}\sum_{\xi,\beta\in\mathcal{S}}\left[\Phi_C^{i-1}(\xi,\eta,\beta;\alpha;t)-\Phi_C^{i-1}(\xi,\alpha,\beta;\eta;t)\right]\ ,$$

$$\begin{aligned}
\frac{d}{dt}\sum_{\beta,\delta\in\mathcal{S}}\mathbb{P}((\alpha,\overset{i}{\beta},\delta)^t)&=\sum_{\eta\in\mathcal{S}\setminus\{\alpha\}}\sum_{\beta,\delta\in\mathcal{S}}\left[\Phi_L^i(\eta,\beta,\delta;\alpha;t)-\Phi_L^i(\alpha,\beta,\delta;\eta;t)\right]\\
&=\sum_{\eta\in\mathcal{S}\setminus\{\alpha\}}\sum_{\xi,\beta\in\mathcal{S}}\left[\Phi_C^{i-1}(\xi,\eta,\beta;\alpha;t)-\Phi_C^{i-1}(\xi,\alpha,\beta;\eta;t)\right]\ .
\end{aligned}$$

Using the same argument, a similar result can be shown for (c). Finally, if condition (d)

hold for $\Pi(t)$, the time derivatives of both sides of (d) coincide. Indeed,

$$\begin{aligned}\frac{d}{dt}\sum_{\delta\in\mathcal{S}}\mathbb{P}((\alpha,\overset{i}{\beta},\delta)^t) &= \sum_{\eta\in\mathcal{S}\setminus\{\alpha\}}\sum_{\delta\in\mathcal{S}}\left[\Phi_L^i(\eta,\beta,\delta;\alpha;t)-\Phi_L^i(\alpha,\beta,\delta;\eta;t)\right]\\ &+\sum_{\eta\in\mathcal{S}\setminus\{\beta\}}\sum_{\delta\in\mathcal{S}}\left[\Phi_C^i(\alpha,\eta,\delta;\beta;t)-\Phi_C^i(\alpha,\beta,\delta;\eta;t)\right]\\ &=\sum_{\eta\in\mathcal{S}\setminus\{\alpha\}}\sum_{\xi\in\mathcal{S}}\left[\Phi_C^{i-1}(\xi,\eta,\beta;\alpha;t)-\Phi_C^{i-1}(\xi,\alpha,\beta;\eta;t)\right]\\ &+\sum_{\eta\in\mathcal{S}\setminus\{\beta\}}\sum_{\delta\in\mathcal{S}}\left[\Phi_C^i(\alpha,\eta,\delta;\beta;t)-\Phi_C^i(\alpha,\beta,\delta;\eta;t)\right]\ ,\end{aligned}$$

$$\begin{aligned}\frac{d}{dt}\sum_{\xi\in\mathcal{S}}\mathbb{P}((\xi,\overset{i-1}{\alpha},\beta)^t) &= \sum_{\eta\in\mathcal{S}\setminus\{\alpha\}}\sum_{\xi\in\mathcal{S}}\left[\Phi_C^{i-1}(\xi,\eta,\beta;\alpha;t)-\Phi_C^{i-1}(\xi,\alpha,\beta;\eta;t)\right]\\ &+\sum_{\eta\in\mathcal{S}\setminus\{\beta\}}\sum_{\xi\in\mathcal{S}}\left[\Phi_R^{i-1}(\xi,\eta,\alpha;\beta;t)-\Phi_R^{i-1}(\xi,\alpha,\beta;\eta;t)\right]\\ &=\sum_{\eta\in\mathcal{S}\setminus\{\alpha\}}\sum_{\xi\in\mathcal{S}}\left[\Phi_C^{i-1}(\xi,\eta,\beta;\alpha;t)-\Phi_C^{i-1}(\xi,\alpha,\beta;\eta;t)\right]\\ &+\sum_{\eta\in\mathcal{S}\setminus\{\beta\}}\sum_{\delta\in\mathcal{S}}\left[\Phi_C^{i}(\alpha,\eta,\delta;\beta;t)-\Phi_C^{i}(\alpha,\beta,\delta;\eta;t)\right]\ .\end{aligned}$$

So we have proved that, provided that $\Pi(t)$ satisfies condition (d), the time derivatives of the left-hand sides of conditions (b)–(d) vanish, which implies hypothesis (20). Therefore we can apply Lemma 1 and conclude that conditions (b)–(d) hold for any $t > 0$. □

References

Amann, H. (1990). *Ordinary differential equations: an introduction to nonlinear analysis*. Vol. 13. Walter de Gruyter.

Araujo, A. and J.W. Walker (1994). "Kinetics of tension development in skinned cardiac myocytes measured by photorelease of Ca2+". In: *American Journal of Physiology-Heart and Circulatory Physiology* 267.5, H1643–H1653.

Backx, P.H., W. Gao, M.D. Azan-Backx, and E. Marbán (1995). "The relationship between contractile force and intracellular [Ca2+] in intact rat cardiac trabeculae." In: *The Journal of General Physiology* 105.1, pp. 1–19.

Bailey, N.T.J. (1990). *The elements of stochastic processes with applications to the natural sciences*. Vol. 25. John Wiley & Sons.

Bers, D. (2001). *Excitation-contraction coupling and cardiac contractile force*. Vol. 237. Springer Science & Business Media.

Brandt, P.W., M.S. Diamond, J.S. Rutchik, and F.H Schachat (1987). "Co-operative interactions between troponin-tropomyosin units extend the length of the thin filament in skeletal muscle". In: *Journal of molecular biology* 195.4, pp. 885–896.

Campbell, S.G., F.V. Lionetti, K.S. Campbell, and A.D. McCulloch (2010). "Coupling of adjacent tropomyosins enhances cross-bridge-mediated cooperative activation in a Markov model of the cardiac thin filament". In: *Biophysical Journal* 98.10, pp. 2254–2264.

Chabiniok, R., V.Y. Wang, M. Hadjicharalambous, L. Asner, J. Lee, M. Sermesant, E. Kuhl, A.A. Young, P. Moireau, M.P. Nash, D. Chapelle, and D.A. Nordsletten (2016). "Multiphysics and multiscale modelling, data–model fusion and integration of organ physiology in the clinic: ventricular cardiac mechanics". In: *Interface Focus* 6.2, p. 20150083.

Cipra, B.A. (1987). "An introduction to the Ising model". In: *American Mathematical Monthly* 94.10, pp. 937–959.

Colli Franzone, P., L.F. Pavarino, and S. Scacchi (2014). *Mathematical cardiac electrophysiology*. Vol. 13. Springer.

Dawid, A.P. (1979). "Conditional independence in statistical theory". In: *Journal of the Royal Statistical Society. Series B (Methodological)*, pp. 1–31.

Dobesh, D.P., J.P. Konhilas, and P.P. de Tombe (2002). "Cooperative activation in cardiac muscle: impact of sarcomere length". In: *American Journal of Physiology-Heart and Circulatory Physiology* 51.3, H1055.

Dobrunz, L.E., P.H. Backx, and D.T. Yue (1995). "Steady-state [Ca2+] i-force relationship in intact twitching cardiac muscle: direct evidence for modulation by isoproterenol and EMD 53998". In: *Biophysical Journal* 69.1, pp. 189–201.

Dupuis, L.J., J. Lumens, .T Arts, and T. Delhaas (2016). "Mechano-chemical Interactions in Cardiac Sarcomere Contraction: A Computational Modeling Study". In: *PLoS Computational Biology* 12.10, e1005126.

Eisenberg, E. and T.L. Hill (1985). "Muscle contraction and free energy transduction in biological systems". In: *Science* 227, pp. 999–1007.

Fink, M., S.A. Niederer, E.M. Cherry, F.H. Fenton, J.T. Koivumäki, G. Seemann, R. Thul, H. Zhang, F.B. Sachse, D. Beard, E.J. Crampin, and N.P. Smith (2011). "Cardiac cell modelling: observations from the heart of the cardiac physiome project". In: *Progress in Biophysics and Molecular Biology* 104.1, pp. 2–21.

Ford, L.E., A.F. Huxley, and R.M. Simmons (1977). "Tension responses to sudden length change in stimulated frog muscle fibres near slack length". In: *The Journal of physiology* 269.2, pp. 441–515.

Fung, Y. (2013). *Biomechanics: mechanical properties of living tissues*. Springer Science & Business Media.

Gao, W.D., P.H. Backx, M. Azan-Backx, and E. Marban (1994). "Myofilament Ca2+ sensitivity in intact versus skinned rat ventricular muscle." In: *Circulation research* 74.3, pp. 408–415.

Gerbi, A., L. Dedè, and A. Quarteroni (2017). "A monolithic algorithm for the simulation of cardiac electromechanics in the human left ventricle". In: *MOX Report 51/2017, Politecnico di Milano*.

Hill, A.V. (1938). "The heat of shortening and the dynamic constants of muscle". In: *Proceedings of the Royal Society of London B: Biological Sciences* 126.843, pp. 136–195.

Hill, T.L., E. Eisenberg, Y.D. Chen, and R.J. Podolsky (1975). "Some self-consistent two-state sliding filament models of muscle contraction". In: *Biophysical journal* 15.4, pp. 335–372.

Hunter, P.J., A.D. McCulloch, and H.E.D.J. Ter Keurs (1998). "Modelling the mechanical properties of cardiac muscle". In: *Progress in Biophysics and Molecular Biology* 69.2, pp. 289–331.

Hussan, J., P.P. de Tombe, and J.J. Rice (2006). "A spatially detailed myofilament model as a basis for large-scale biological simulations". In: *IBM journal of research and development* 50.6, pp. 583–600.

Huxely, A. F. (1957). "Muscle structure and theories of contraction". In: *Prog Biophys Biophys Chem*, pp. 255–318.

Huxely, A. F. and R. Niedergerke (1954). "Structural Changes in Muscle During Contraction: Interference Microscopy of Living Muscle Fibres". In: *Nature* 173.4412, pp. 971–973.

Huxely, H. and J. Hanson (1954). "Changes in the Cross-Striations of Muscle during Contraction and Stretch and their Structural Interpretation". In: *Nature* 173.4412, pp. 973–976.

Janssen, P.M. and W.C. Hunter (1995). "Force, not sarcomere length, correlates with prolongation of isosarcometric contraction". In: *American Journal of Physiology - Heart and Circulatory Physiology* 269.2, H676–H685.

Janssen, P.M. and P.P. de Tombe (1997). "Uncontrolled sarcomere shortening increases intracellular Ca2+ transient in rat cardiac trabeculae". In: *American Journal of Physiology - Heart and Circulatory Physiology* 272.4, H1892–H1897.

Keener, J.P. and J. Sneyd (2009). *Mathematical Physiology*. Vol. 1. Springer.

Kentish, J.C., H.E.D.J. ter Keurs, L. Ricciardi, J.J.J. Bucx, and M.I.M. Noble (1986). "Comparison between the sarcomere length-force relations of intact and skinned trabeculae from rat right ventricle. Influence of calcium concentrations on these relations." In: *Circulation research* 58.6, pp. 755–768.

Land, S. and S.A. Niederer (2015). "A spatially detailed model of isometric contraction based on competitive binding of troponin I explains cooperative interactions between tropomyosin and crossbridges". In: *PLoS Computational Biology* 11.8, e1004376.

Land, S., S. Park-Holohan, N.P. Smith, C.G. dos Remedios, J.C. Kentish, and S.A. Niederer (2017). "A model of cardiac contraction based on novel measurements of tension development in human cardiomyocytes". In: *Journal of Molecular and Cellular Cardiology* 106, pp. 68–83.

Landesberg, A. and S. Sideman (1994). "Coupling calcium binding to troponin C and cross-bridge cycling in skinned cardiac cells". In: *American Journal of Physiology-Heart and Circulatory Physiology* 266.3, H1260–H1271.

Niederer, S A, P J Hunter, and N P Smith (2006). "A quantitative analysis of cardiac myocyte relaxation: a simulation study". In: *Biophysical Journal* 90.5, pp. 1697–1722.

Norris, J.R (1998). *Markov chains*. 2. Cambridge university press.

Pate, E. and R. Cooke (1986). "A model for the interaction of muscle cross-bridges with ligands which compete with ATP". In: *Journal of theoretical biology* 118.2, pp. 215–230.

Quarteroni, A., T. Lassila, S. Rossi, and R. Ruiz-Baier (2017). "Integrated Heart–Coupling multiscale and multiphysics models for the simulation of the cardiac function". In: *Computer Methods in Applied Mechanics and Engineering* 314, pp. 345–407.

Razumova, M.V., A.E. Bukatina, and K.B. Campbell (1999). "Stiffness-distortion sarcomere model for muscle simulation". In: *Journal of Applied Physiology* 87.5, pp. 1861–1876.

Rice, J.J. and P.P. de Tombe (2004). "Approaches to modeling crossbridges and calcium-dependent activation in cardiac muscle". In: *Progress in Biophysics and Molecular Biology* 85.2, pp. 179–195.

Rice, J.J., R.L. Winslow, and W.C. Hunter (1999). "Comparison of putative cooperative mechanisms in cardiac muscle: length dependence and dynamic responses". In:

American Journal of Physiology-Heart and Circulatory Physiology 276.5, H1734–H1754.

Rice, J.J., G. Stolovitzky, Y. Tu, and P.P. de Tombe (2003). "Ising model of cardiac thin filament activation with nearest-neighbor cooperative interactions". In: *Biophysical Journal* 84.2, pp. 897–909.

Rice, J.J., F. Wang, D.M. Bers, and P.P. de Tombe (2008). "Approximate model of cooperative activation and crossbridge cycling in cardiac muscle using ordinary differential equations". In: *Biophysical Journal* 95.5, pp. 2368–2390.

Rossi, S., T. Lassila, R. Ruiz-Baier, A. Sequeira, and A. Quarteroni (2014). "Thermodynamically consistent orthotropic activation model capturing ventricular systolic wall thickening in cardiac electromechanics". In: *European Journal of Mechanics-A/Solids* 48, pp. 129–142.

Ruiz-Baier, R., A. Gizzi, S. Rossi, C. Cherubini, A. Laadhari, S. Filippi, and A. Quarteroni (2014). "Mathematical modelling of active contraction in isolated cardiomyocytes". In: *Mathematical Medicine and Biology* 31.3, pp. 259–283.

Sachse, F.B. (2004). *Computational Cardiology: Modeling Of Anatomy, Electrophysiology, And Mechanics (Lecture Notes In Computer Science)*. Secaucus, NJ, USA: Springer-Verlag New York, Inc.

Sachse, F.B., K.G. Glänzel, and G. Seemann (2003). "Modeling of protein interactions involved in cardiac tension development". In: *International Journal of Bifurcation and Chaos* 13.12, pp. 3561–3578.

Tombe, P.P. de and G.J.M. Stienen (1997). "The rate of tension redevelopment in rat cardiac muscle: Influence of temperature and contractile activation level". In: *Circulation*. Vol. 96. 8, pp. 2900–2900.

Trayanova, N.A. and J.J. Rice (2011). "Cardiac electromechanical models: from cell to organ". In: *Frontiers in physiology* 2, p. 43.

Washio, T., J. Okada, S. Sugiura, and T. Hisada (2012). "Approximation for cooperative interactions of a spatially-detailed cardiac sarcomere model". In: *Cellular and Molecular Bioengineering* 5.1, pp. 113–126.

Washio, T., J. Okada, A. Takahashi, K. Yoneda, Y. Kadooka, S. Sugiura, and T. Hisada (2013). "Multiscale heart simulation with cooperative stochastic crossbridge dynamics and cellular structures". In: *Multiscale Modeling & Simulation* 11.4, pp. 965–999.

Washio, T., K. Yoneda, J. Okada, T. Kariya, S. Sugiura, and T. Hisada (2015). "Ventricular fiber optimization utilizing the branching structure". In: *International Journal for Numerical Methods in Biomedical Engineering*.

Wolff, M.R., K.S. McDonald, and R.L. Moss (1995). "Rate of tension development in cardiac muscle varies with level of activator calcium". In: *Circulation Research* 76.1, pp. 154–160.

Wong, A.Y.K. (1971). "Mechanics of cardiac muscle, based on Huxley's model: mathematical simulation of isometric contraction". In: *Journal of biomechanics* 4.6, pp. 529–540.

MOX Technical Reports, last issues

Dipartimento di Matematica
Politecnico di Milano, Via Bonardi 9 - 20133 Milano (Italy)

47/2017 Menghini, F.; Dede, L.; Forti, D.; Quarteroni, A.
Hemodynamics in a left atrium based on a Variational Multiscale-LES numerical model

46/2017 Agosti, A.; Gower, A.L.; Ciarletta, P.
The constitutive relations of initially stressed incompressible Mooney-Rivlin materials

45/2017 Gasperoni, F.; Ieva, F.; Paganoni, A.M.; Jackson C.H.; Sharples L.D.
Nonparametric frailty Cox models for hierarchical time-to-event data

43/2017 Bottle, A.; Ventura, C.M.; Dharmarajan, K.; Aylin, P.; Ieva, F.; Paganoni, A.M.
Regional variation in hospitalisation and mortality in heart failure: comparison of England and Lombardy using multistate modelling

44/2017 Martino, A.; Ghiglietti, A.; Ieva, F.; Paganoni, A.M.
A k-means procedure based on a Mahalanobis type distance for clustering multivariate functional data

42/2017 Gower, AL, Shearer, T, Ciarletta P
A new restriction for initially stressed elastic solids

41/2017 Beretta, E.; Micheletti, S.; Perotto, S.; Santacesaria, M.
Reconstruction of a piecewise constant conductivity on a polygonal partition via shape optimization in EIT

37/2017 Formaggia, L.; Vergara, C.; Zonca, S.
Unfitted Extended Finite Elements for composite grids

38/2017 Bonaventura, L.; Fernandez Nieto, E.; Garres Diaz, J.; Narbona Reina, G.;
Multilayer shallow water models with locally variable number of layers and semi-implicit time discretization

39/2017 Ciarletta, P.
Matched asymptotic solution for crease nucleation in soft solids